ACS OMEGA

Open Access

http://pubs.acs.org/journal/acsodf

Article

Structural Growth Pattern, Electronic Configurations, and Spectral and Thermochemistry Properties of $ZrSn_n^{0/-/2-}$ (n = 4−17) Nanoscale Compounds: A Systematic Study Using Density Functional Theory

Yanpeng Zhang, Jucai Yang, and Caixia Dong*

Cite This: *ACS Omega* 2024, 9, 3675−3690

Read Online

ACCESS | Metrics & More | Article Recommendations | Supporting Information

ABSTRACT: By performing density functional theory (DFT) calculations for geometric optimization in conjunction with the artificial bee colony algorithm for cluster (ABCluster) global search approach, the ground-state structures of the neutral, anionic, and dianionic $ZrSn_n^{0/-/2-}$ (n = 4−17) nanoscale compounds are obtained. Their structural growth evolution, spectral information, and electronic and thermochemical properties are investigated. Regarding the architectural evolution of the neutral, anion, and dianionic species, $ZrSn_n^{0/-/2-}$ (n = 4−17) compounds possess two different stages of adsorption patterns in which, when n = 4−7 and n = 8−17, $ZrSn_4^{0/-/2-}$ and $ZrSn_8^{0/-/2-}$ compounds as the basic motif adsorb Sn atoms to become the larger clusters, respectively. The simulated photoelectron spectra (PES) of anionic compounds are in good agreement with the available experimental PES. The infrared and Raman spectra can be summarized as follows: under infrared vibrational modes, the sealed cages of $ZrSn_n^{0/-/2-}$ compounds belong to the deformation mode, and under Raman vibrational modes, they belong to the breathing mode of the Sn cage framework. The density of states (DOS) spectra and natural population analysis (NPA) indicate that the interaction between the Zr atom and Sn_n frameworks of capsulated compounds has been developing stronger than for unsealed compounds. The results of thermochemical properties, molecular orbital shell (MOs) analysis, and ultraviolet−visible (UV−vis) absorption spectrum indicate that the neutral $ZrSn_{16}$ nanoscale compound possesses not only both thermodynamic and chemical stability but also far-infrared sensing and optoelectronic properties and hence, is the best building block motif for new multipurpose nanoscale materials.

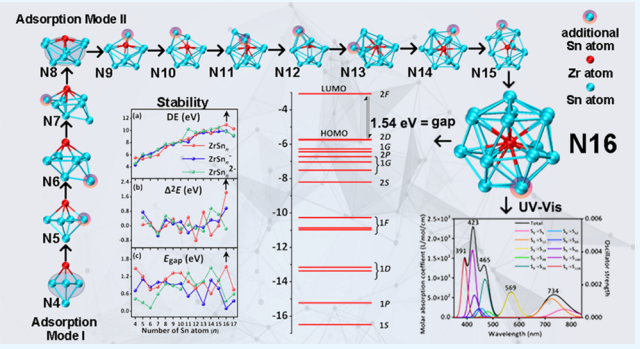

1. INTRODUCTION

Since the discovery of the buckminster fullerene C_{60} structure of the carbon group, the unique geometries, analogous and diverse physicochemical and structural properties of the heavy congeners of carbon Si, Ge, Sn, and Pb, as well as their wide range of applications in nanotechnology and electronics industries have resulted in their being surprisingly hot spots for nanoscale research in cluster science.[1−11] Especially, the stannum element shows the α-phase (gray diamond cubic structure having a covalent nature) and β-phase (white body-centered tetragonal structure with a metallic nature), existing as a transition from semiconductor to metal in the carbon group. These unique characteristics of the transition endow the stannum element with a low melting point, nontoxicity, high corrosion resistance, good ductility, and wettability, leading to its wide application in industries such as electronics, electrical appliances, metallurgy, machinery, building materials, chemical engineering, and others. As a result, researchers have studied the composition, atomic arrangement, and cluster size of tin clusters to investigate the effect of tin clusters on their physical and chemical properties.[12−17] Furthermore, with the rapid development and wide application of nanotechnology, atomic clusters serve as a bridge between the microscopic atomic molecules and macroscopic condensed matter. In particular, transition metal (TM)-doped tin alloys are used in the atomic energy industry, aviation industry, superconducting materials, spacecraft manufacturing, and other cutting-edge technology fields.

Introducing transition metal atoms to tin clusters has attracted many studies due to the fact that the interaction between the transition metal atom and the tin cluster can range from strongly covalent all the way to cases where the metal is simply trapped inside the cage by virtue of the strong Sn−Sn bonds, with little or no direct bonding. These specific bond types are used to develop unusual structural architectures and

Received: October 3, 2023
Revised: November 29, 2023
Accepted: December 27, 2023
Published: January 12, 2024

evolution, and spectroscopic and magnetic properties.[18] As a result, there are many studies investigating the ground-state configurations of TM-doped Sn clusters, and their structural growth behavior, electronic structures, as well as spectra and stability properties to understand the construction units of tunable functional materials and devices. For instance, on the theoretical aspect, the ground-state structures of $FeSn_x$ (x = 1−8) small clusters and their magnetic properties were investigated using the PBE scheme,[19] from which it was concluded that the presence of the Fe impurity modifies the most stable geometries and the spin state of the free Sn clusters. The structural and electronic properties of $TiSn_x^{-/0/+}$ and $AlSn_x^{-/0/+}$ (x = 1−10) small clusters were calculated using B3PW91 and B3LYP density functional theory, respectively.[20,21] The equilibrium geometries and electronic properties of TM_xSn_y (TM = Fe, Co, Ni; $x + y \leq 5$) clusters were investigated at the PBE level by Sosa-Hernández et al.,[22−24] who reported that the most stable structures of these clusters prefer motifs with high coordination and differ from those of the pure clusters, and that all of the clusters exhibit a magnetic behavior independently of the TM concentration. The $TMX_{10}^{+/0/-}$ (TM = Cu, Ag, Au; X = Ge, Sn, Pb) and the $ZnSn_x$ (x = 1−12) clusters were studied using B3LYP and CCSD(T) theory by Tai et al.,[25−27] and it was found that the enhanced stability of $CuX_{10}^{\pm}$, $AuX_{10}^{\pm}$, $ZnSn_{10}$, and $ZnSn_{12}$ magic clusters can be rationalized by the three-dimensional aromaticity. Recently, $Au@X_{12}$ (X = Ge, Sn, Pb) and their anions were explored using the B3LYP scheme by Zhang et al.,[28] who found that $Au@Sn_{12}$ and $Au@Pb_{12}$ clusters possess the perfect icosahedral structure and high chemical stabilities because of their spherical aromaticity. On the experimental aspect, the mass abundance spectra of binary TM-doped semimetal (SM) $TMSM_x$ (SM = Si, Ge, Sn, Pb, and TM = Cr, Mn, Cu, Zn) clusters were recorded by Neukermans et al.,[29] who interpreted the enhanced abundance of several sizes on the basis of the peculiarly stable dopant-encapsulated structures. A mass spectrometry and molecular beam magnetic deflection experiment for manganese-doped tin clusters was performed by Rohrmann et al.,[30] who found that the size of the smallest Mn-encapsulated Sn_x configurations is x = 10, and that the magnetic dipole moments for $Mn@Sn_{12}$ are in close accordance with the spin quantum number S = 5/2 predicted by theoretical computation.[31] This conclusion was also confirmed by later electron beam deflection and magnetic double deflection experiments.[32,33] The magnetic response of the $Fe@Sn_{12}$ cluster in the magnetic beam deflection experiments was investigated by Rohrmann et al.,[34] who concluded that in contrast to $Mn@Sn_{12}$, the molecular beam of the $Fe@Sn_{12}$ cluster does not show superatomic paramagnetic response due to Jahn−Teller induced distortions of the Sn cage. Recently, the geometric and electronic structures of $AuSn_x$ and $CuSn_x$ (x = 6−16) nanoalloy clusters were studied using a molecular beam magnetic deflection experiment combined with a genetic algorithm based on density functional theory by Gleditzsch et al.,[35,36] who confirmed that the size of the smallest Au- and Cu-encapsulated Sn_x configurations is x = 9. The photoelectron spectra (PES) of anionic $TMGe_x$ (TM = Sc, Y, Ti, Zr, Hf, V, Nb, Ta, and Lu) and $TMSn_x$ (TM = Sc, Y, Ti, Zr, and Hf) were recorded by Nakajima and co-workers[37,38] to investigate their structural and electronic properties outside of the molecular beam magnetic deflection experiment.

Albeit the photoelectron spectroscopy of anionic $ZrSn_n$ for specific sizes such as n = 15−17 species recorded by Nakajima and co-workers,[37,38] at present there is still a lack of theoretical studies on the ground-state geometry and electronic characteristics after introducing Zr atoms into small- and medium-sized stannum clusters. The four main sections in this article aim to tackle several challenges in order to investigate Zr-doped stannum clusters: (i) It is a big challenge to find the reliable global minimum structures from the initial geometry without a global search technique, even for small clusters. The various properties of Zr-doped Sn clusters can hardly be interpreted without understanding the conformational growth model. Thus, the ABCluster technique, a trustworthy approach for searching complete initial isomers, is used as the foundation, and subsequently, the optimizing calculation scheme is used to verify the applicability and correctness by comparing with experimental data. Moreover, unlike Si or Ge clusters, spin multiplicities of TM-doped Sn clusters are needed to consider all possible spin multiplicities since the TM atom is introduced into the Sn-sealed cage and the TM-Sn bonds probably range from rarely interacting all the way to strongly covalent.[18] (ii) Up to now, there is no existing experimental method to directly analyze the ground-state structure of clusters. As a result, through a comparison of computed and experimental spectra for indirectly obtaining the structural information and proving the computational method reliable, such as PES, infrared, or Raman spectra, the global minimal structures can be indirectly assessed effectively for indirectly providing the structural information for the future experimental researches about this species. (iii) Exploring the interaction between Zr atom and Sn clusters in the small and medium-sized ZrSn clusters, such as total density of states (TDOS) and partial (PDOS) density of states and charge transfer, is essential to understanding the structural evolution of clusters since the electrical structure of clusters, which is the deciding element for their physical and chemistry characteristics, is directly related to their geometric configuration. (iv) From the small- and medium-sized Zr atom-doped stannum cluster system, a material building block with great symmetry and stability that can be employed as a novel multifunctional material is retrieved. So, all said, in this work, the ABCluster global search approach coupled with density functional theory (DFT) was employed for the structure optimization of $ZrSn_n^{0/-/2-}$ (n = 4−17) clusters with the objective of determining their structural evolution, exploring their electronic structures and properties, obtaining insight into their bonding characteristics, and furnishing substantial information for in-depth research on other transition metals' doping with semiconductor clusters.

2. COMPUTATIONAL METHODS

All calculations were employed in the Gaussian 09 program package.[39] There are three phases for searching the global minimum structures. The first phase involves collecting a large amount of initial configurations from the three approaches that were performed to obtain a large amount of initial configurations, to avoid missing the true global minima of $ZrSn_n^{0/-/2-}$ (n = 4−17) compounds. First, the ABCluster global search approach,[40−42] which possesses important functions such as its unique "artificial bee colony" algorithm to perform the global optimization with proper potential energy functions and its role as a random generator when combined with the Gaussian 09 code, was utilized for searching 100 isomers when n = 4−6, 300 isomers when n =

https://doi.org/10.1021/acsomega.3c07674
ACS Omega 2024, 9, 3675−3690

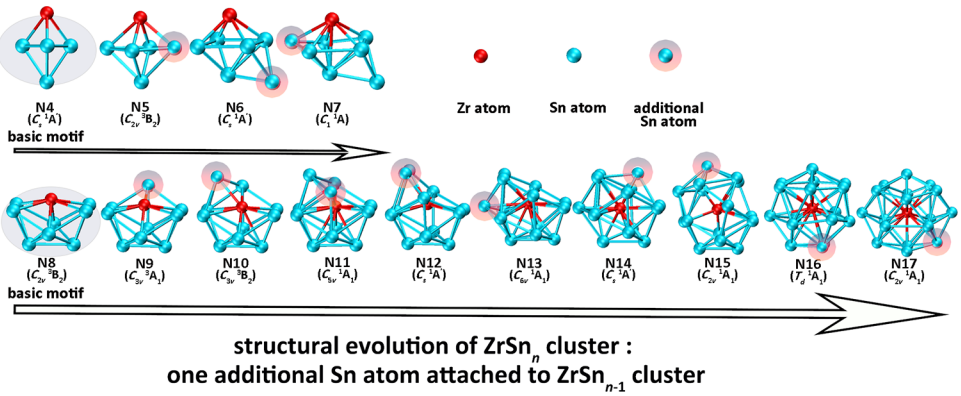

Figure 1. Most stable geometries of neutral $ZrSn_n$ (n = 4−17) species and structural evolution.

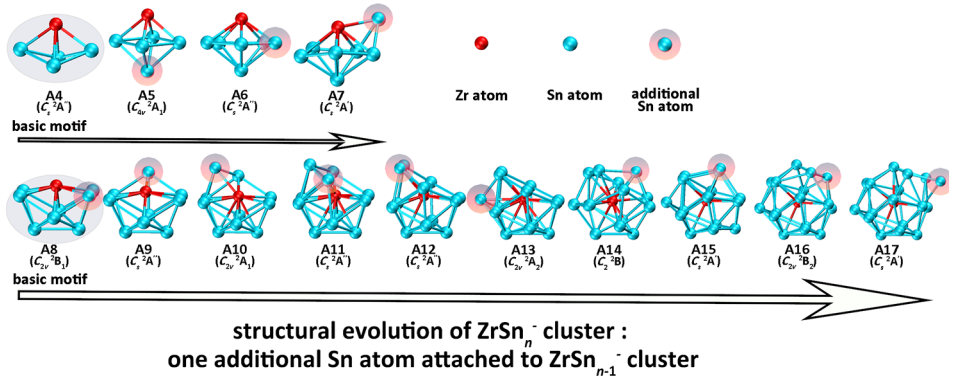

Figure 2. Most stable geometries of anionic $ZrSn_n^-$ (n = 4−17) species and structural evolution.

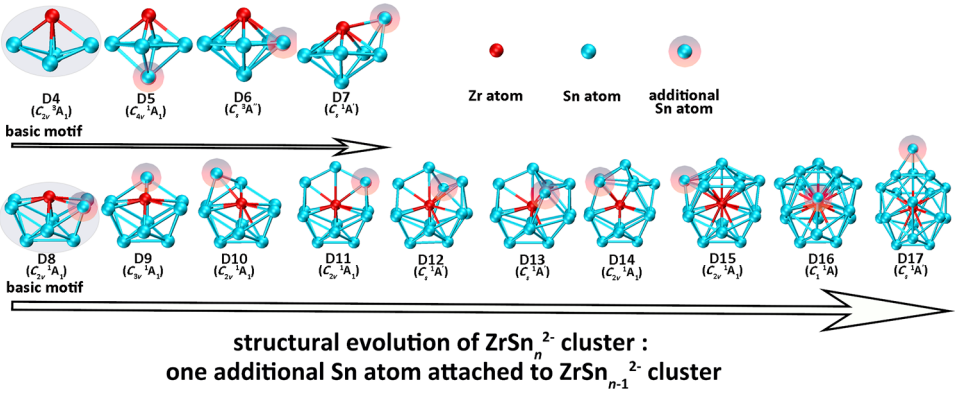

Figure 3. Most stable geometries of dianionic $ZrSn_n^{2-}$ (n = 4−17) species and structural evolution.

7−10, and 400 isomers when n = 11−17 by the PBE0[43] functional associated with the relativistic effective core pseudopotential basis set cc-pVDZ-PP for Zr atoms and the effective core potential basis set LanL2DZ[44,45] for Sn atoms. The "substitution geometries" was the second approach, used to replace one Sn atom in the Sn_{n+1} compound with the Zr atom. The third approach that was executed selects the configurations that have already been published in the previous literature as supplements.[2−4,18−28] For the second phase, these initial isomers were then further optimized at PBE0,[43] B3LYP,[46,47] and CAM-B3LYP[48] functionals, respectively, which provided reliable results.[49−51] Considering the high computational costs and accuracy,[52−54] we chose the triple-ζ LANL2TZ[44,55] basis set for the Zr atom, which is provided with a quasi-relativistic effective core potential, and the cc-pVTZ-PP[56,57] basis set for the Sn atom, which is provided with a relativistic effective core pseudopotential. Symmetry constraints were not presented during this process. Meanwhile, it is essential to calculate their harmonic vibration frequencies along with the optimizing process, because their positive value of frequencies can ensure the generation of low-lying structures corresponding to the true local minima. After completion of the geometry optimization through the second phase, low-lying structures of $ZrSn_n^{0/-/2-}$ (n = 4−17) compounds were generated for single-point energy calculations for the third phase in order to further refine the energy at PBE0,[43] B3LYP[46,47] and CAM-B3LYP[48] functionals coupled with LANL2TZ[44,55] for Zr and aug-cc-pVTZ-PP[56,57] for Sn. To calculate PES based on the generalized Koopmans' theorem,[58,59] infrared and Raman, NPA, DOS, and the stability of

https://doi.org/10.1021/acsomega.3c07674
ACS Omega 2024, 9, 3675−3690

the lowest-energy configurations of $ZrSn_n^-$ (n = 4−17) compounds at PBE0 functional were investigated, and the PES calculated at PBE0, B3LYP, and CAM-B3LYP functionals for n = 15−17 were compared with the experimental spectra. The results obtained by PBE0, B3LYP, and CAM-B3LYP functionals (see Supporting Information) for the ground-state structures, the energy order of the low-energy structures, and simulated PES compared with the experiments were in coincidence with each other, and the discussion below is only based on the PBE0 functional. The simulated PES, DOS curves, and ultraviolet−visible (UV−vis) spectra were used to analyze the wave functions by Multiwfn code,[60] and the global and local minimum structures, MOs, and vibrational modes were visualized using the VMD[61] software. For $ZrSn_n^{0/-/2-}$ with n = 4−17, the spin multiplicities of singlet and triplet for neutral and dianion were taken into account, and those of doublet and quartet for the anion; those that resulted from the ground states of Sn_n with n = 4−17 were predicted to be singlet.[9] Our results revealed that the ground state of the anion with n = 4−17 is doublet, that of neutral is singlet except for n = 5, 8−10, and that of dianion is singlet except for n = 4 and 6.

3. RESULTS AND DISCUSSION

3.1. Ground-State Structures and Growth Evolutions of $ZrSn_n^{0/-/2-}$ (n = 4−17) Species. As exhibited in Figures 1, 2 and 3, the equilibrium configurations and point group of zirconium-doped tin $ZrSn_n^{0/-/2-}$ (n = 4−17) species and their growth evolution are separately displayed in the three figures classified as neutral, anion, and dianion. The local minimal configurations by PBE0, B3LYP, and CAM-B3LYP functionals are shown in Figures S1−S3. The reported configurations are marked as **N*n*-*x***, **A*n*-*x***, and **D*n*-*x***, in which **N**, **A**, and **D** represent neutral, anion, and dianion, respectively; ***n*** is the number of Sn atoms and ***x*** is the number of energetic rank from low to high. In Figures 1−3, the equilibrium configurations are labeled as **N*n***, **A*n***, and **D*n***. For neutral species, the most stable configuration of $ZrSn_4$ is the triangular bipyramid configuration named **N4**, which can be viewed as the Zr atom capping one face of the distorted Sn_4-tetrahedron, with C_s-symmetry and $^1A'$ electron state. **N5** is the tetragonal bipyramid configuration having C_{2v}-symmetry and $^3B_2$ electron state, in which the Zr atom is located at the top vertex of the chief axis, and also can be regarded as attaching one Sn atom on the side face of **N4**. The ground state of **N5** is the triplet state, possessing more stable energies of 0.19, 0.05, and 0.08 eV than the corresponding singlet state at PBE0, B3LYP, and CAM-B3LYP functionals, respectively. **N6** has a capping tetragonal bipyramid configuration with C_s-symmetry and $^1A'$ electron state, and can be described as capping one Sn atom on one face of **N5**. **N7** can be viewed as a face-capped distorted pentagonal bipyramid or can be served as absorbing one Sn atom to the Sn_4-quadrangle of **N6**, forming a five-membered ring of **N7**.

Beginning with n = 8, the species form the semiendohedral architecture. **N8** is treated as attaching two Sn atoms on the two adjacent faces of the distorted pentagonal bipyramid, respectively (boat-like skeleton), with C_{2v}-symmetry and $^3B_2$ electron state. It has triplet state, possessing more stable energies of 0.13, 0.17, and 0.58 eV than the corresponding singlet state at PBE0, B3LYP, and CAM-B3LYP functionals, respectively. **N9** is in C_{3v}-symmetry and has the $^3A_1$ electron state, and can be depicted as adding one Sn atom on **N8**. **N9** possesses less energies of 0.17, 0.35, and 0.57 eV at triplet state than the corresponding singlet state at PBE0, B3LYP, and CAM-B3LYP functionals, respectively. **N10** possesses C_{3v}-symmetry and $^3B_2$ electron state and can be depicted as adding one Sn atom on **N9**. The triplet state of **N10** has less energies of 0.25, 0.14, and 0.86 eV than the corresponding singlet state at PBE0, B3LYP, and CAM-B3LYP functionals, respectively. As for $ZrSn_{11}$, the lowest-energy geometry **N11** is the Zr-centered capped antipentagonal prism (yurt-like skeleton), which is regarded as based on **N10** for one more Sn atom. It has C_{5v}-symmetry and $^1A_1$ electron state and is the complete cage framework because of the Zr atom at the center of the antipentagonal prism of the yurt-like framework, whereas the Zr atom is not completely sealed into the tin skeleton when n = 10. In other words, from n = 8 to 10, the Zr atoms become increasingly encircled by the Sn_n skeleton, and beginning with n = 11, the neutral species veritably develop sealed architectures. Interestingly, **N9**, **N10**, and **N11** can be treated as each adding one, two, and three Sn atoms on one, two, and three nearby faces of **N8**, respectively. **N12**, with C_s-symmetry and $^1A'$ electron state, is the capping antihexagonal-pentagonal prism, which can be regarded as absorbing one Sn atom to the five-membered ring of **N11**, forming a six-membered ring of **N12**. As for **N13**, the capping antihexagonal prism has C_{6v}-symmetry and $^1A_1$ electron state, and can be viewed as absorbing one Sn atom to the five-membered ring of **N12**, forming a six-membered ring of **N13**. **N14** is the bicapped antihexagonal prism capping one Sn atom to the top of **N13** and possesses C_s-symmetry and $^1A'$ electron state. Interestingly, **N12**, **N13**, and **N14** each attach four, five, and six Sn atoms on **N8**, respectively. The tricapped antihexagonal prism geometry (**N15**), with C_{2v}-symmetry and $^1A_1$ electron state, is sighted as one Sn atom attached to **N14**. It also can be sighted as covering one capping five-membered ring and one Sn atom on **N8**. **N16** is the Zr-centered Sn_{16} FK-cage with T_d-symmetry and $^1A_1$ electron state, and can be viewed as one more Sn atom on **N15**. It also can be viewed as covering one capping six-membered ring and one Sn atom on **N8**. **N17** can also be regarded as absorbing one Sn atom on the FK-cage framework (**N16**) with extending distorted C_{2v}-symmetry and $^1A_1$ electron state. It can also be regarded as covering one capping five-membered ring and three Sn atoms on **N8**. The architectural growth pattern of the neutral species can be summarized thus: the $ZrSn_n$ (n = 4−17) compounds possess two different types of adsorption pattern. The $ZrSn_4$ compound as the beginning of the basic architecture adsorbs an additional Sn atom on different locations of the prior architecture to be the larger cluster from n = 4 to 7, while at n = 8−17, the $ZrSn_8$ cluster as the beginning of the basic architecture adsorbs an additional Sn atom on different locations of the prior architecture one by one until one Sn atom gets adsorbed on the FK-cage framework for **N17**.

For anions, the equilibrium geometry of the $ZrSn_n^-$ (n = 4−17) species resembles that of their corresponding neutrals (except n = 4, 6, 7, 14, and 17). **A4** is the triangular bipyramid in which the Zr atom is capped on the distorted Sn_4-rhombus, with C_s-symmetry and $^2A''$ electron state. **A6** keeps the pentagonal bipyramid structure in which the Zr atom is at the top vertex of the chief axis, regarded as absorbing one Sn atom to the quadrangle of **A5**, forming a pentagon of **A6** with C_s-symmetry and $^2A''$ electron state. **A7** can be viewed as attaching one Sn atom at the top face of the pentagonal bipyramid (**A6**). Compared with **N14**, **A14** geometry is Zr-centered into the distorted bicapping antihexagonal prism with

https://doi.org/10.1021/acsomega.3c07674
ACS Omega 2024, 9, 3675−3690

Table 1. Theoretical and Experimental AEA (in eV) and VDE (in eV) for the Most Stable $ZrSn_n$ (n = 4−17) Species

	AEA				VDE			
	theor.				theor.			
n	PBE0	B3LYP	CAM-B3LYP	exp.	PBE0	B3LYP	CAM-B3LYP	exp.
N4 ← A4	1.71	1.67	1.80		2.15	2.23	2.11	
N5 ← A5	2.47	2.52	2.48		2.65	2.65	2.68	
N6 ← A6	2.54	2.43	2.40		2.77	2.66	2.81	
N7 ← A7	2.60	2.55	2.60		2.94	2.86	2.92	
N8 ← A8	2.85	2.82	2.87		2.87	2.84	2.90	
N9 ← A9	2.76	2.73	2.79		2.79	2.77	2.82	
N10 ← A10	2.93	2.93	2.97		3.00	2.99	3.05	
N11 ← A11	2.51	2.44	2.51		2.70	2.72	2.88	
N12 ← A12	2.94	2.83	2.86		3.23	3.12	3.19	
N13 ← A13	2.59	2.47	2.51		2.66	2.58	2.60	
N14 ← A14	3.07	2.96	3.07		3.39	3.27	3.43	
N15 ← A15	2.73	2.58	2.64	2.70 ± 0.05[a]	2.92	2.79	2.87	3.11 ± 0.10[a]
N16 ← A16	2.14	2.16	2.11	2.06 ± 0.05[a]	2.19	2.21	2.16	2.25 ± 0.10[a]
N17 ← A17	2.42	2.35	2.46	2.45 ± 0.05[a]	2.60	2.58	2.61	4.04 ± 0.10[a]

[a]The experimental data were taken from ref 38.

extended distortion, possessing C_2-symmetry and ^{2}B electron state, or can be regarded as a Sn atom attached to the pentagon of **A13**. **A17**, with C_s-symmetry and ^{2}A′ electron state, can be viewed as attaching one Sn atom to the face of FK-cage **A16**, in which one Sn atom is pushed outside from the framework, probably due to the exceeded threshold size of matching of the two atomic sizes for one more Sn atom than **A16** or one more electron than **N17**.

As for dianions, the equilibrium geometry of the $ZrSn_n^{2-}$ (n = 4−17) species resembles that of their corresponding anions except the **D11**, **D13**, and **D15**. **D11**, possessing C_{2v}-symmetry and ^{1}A$_1$ electron state, is viewed as attaching additional one Sn atom with **D10**, and also can attach three Sn atoms linearly covered on the top of **D8**, forming **D11**. **D13**, possessing C_s-symmetry and ^{2}A′ electron state, is viewed as attaching additional one Sn atom with **D12**, which also can cover one Sn atom and a tetrahedron on **D8**. **D15**, possessing C_{2v}-symmetry and ^{1}A$_1$ electron state, is viewed as attaching an additional Sn atom with **D14**, which also can cover a one-atom-capping six-membered ring on the **D8**. Apart from this, the triplet state of **D4** has less energies of 0.02, 0.16, and 0.03 eV than the corresponding singlet state at PBE0, B3LYP, and CAM-B3LYP functionals, respectively. The ground state of **D6** is the triplet state, possessing more stable energies of 0.07, 0.01, and 0.09 eV than the corresponding singlet state at PBE0, B3LYP, and CAM-B3LYP functionals, respectively. Concentrating on the architectural growth pattern of anions and dianions, starting from n = 4, anionic and dianionic clusters can be depicted as, from $ZrSn_4$ compound as the beginning of the basic architecture, adding an additional Sn atom on different locations of the prior architecture to be the larger cluster one by one until n = 17. Furthermore, $ZrSn_n^{-/2-}$ (n = 4−17) compounds also possess two different types of adsorption pattern in which $ZrSn_4^{-/2-}$ and $ZrSn_8^{-/2-}$ clusters as the basic motif adsorb Sn atoms on different locations of the prior architecture to be the larger cluster, for n = 4−7 and n = 8−17, respectively. Among these, $ZrSn_8^{-/2-}$, $ZrSn_9^{-/2-}$, $ZrSn_{10}^{-/2-}$, $ZrSn_{11}^{2-}$, and $ZrSn_{12}^{2-}$ compounds have semiencapsulated structures. That is to say, up to $ZrSn_{11}^-$ and $ZrSn_{13}^{2-}$ compounds, the Zr atoms are completely encircled in the tin skeletons.

3.2. Spectral Information: PES, Infrared, and Raman.

Since a little change of the geometric and electronic configuration clusters can result in distinctly different peak shapes of the spectra, such as PES, infrared, and Raman, spectral information can indirectly be validated for the global minimal structures. The vertical detachment energy (VDE) and adiabatic electron affinity (AEA) calculations, corresponding to assessments of the location of the first peak and the rising edge of the first peak in the measured spectrum, are two benchmarks utilized to compare the simulated and experimental PES. The other benchmark concerns the location and number of peaks between the two types of spectra.

The AEA value is the energy difference between the global minimal configurations of neutral and anion, and the VDE value is the energy difference between the anionic global minimal configuration of neutral and anion

$$E_{\mathrm{AEA}} = E_{(\mathrm{optimizedneutral})} - E_{(\mathrm{optimizedanion})} \quad (1)$$

$$E_{\mathrm{VDE}} = E_{(\mathrm{neutralatoptimizedanionicstructure})} - E_{(\mathrm{optimizedanion})} \quad (2)$$

The VDE and AEA computed at PBE0, B3LYP, and CAM-B3LYP functionals, and experimentally measured values are presented in Table 1. On comparing the theoretical AEA of $ZrSn_n^-$ (n = 15−17) with the available experimental values, they are found to be consistent with each other, and their mean absolute error is 0.047, 0.107, and 0.040 eV at PBE0, B3LYP and CAM-B3LYP functionals, respectively. The mean absolute error of the calculated VDE of $ZrSn_n^-$ (n = 15−17) is 0.563, 0.607, and 0.587 eV at PBE0, B3LYP, and CAM-B3LYP functionals, respectively, compared with the available measured data. On removing the largest deviation (1.44, 1.46, and 1.43 eV corresponding to the three functionals) belonging to $ZrSn_{17}^-$, the VDE value's mean absolute error is only 0.125, 0.180, and 0.165 eV at PBE0, B3LYP, and CAM-B3LYP functionals, respectively. Such deviation of the VDE at n = 17 for the three DFT methods possibly may have been caused by the technical limitations that buried the two low-intensity peaks when the experimental spectrum of $ZrSn_{17}^-$ was published in earlier years. It also can be observed from measured PES as below. The AEA at n = 17, which estimates the rising edge of the first peak, and the VDE at n = 17, which

https://doi.org/10.1021/acsomega.3c07674
ACS Omega 2024, 9, 3675−3690

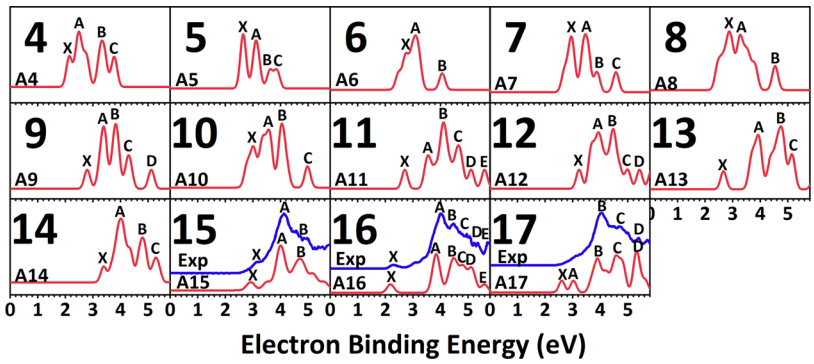

Figure 4. Simulated PES of the most stable anionic $ZrSn_n^-$ (n = 4−17) species; experimental photoelectron spectra are taken from reference 38.

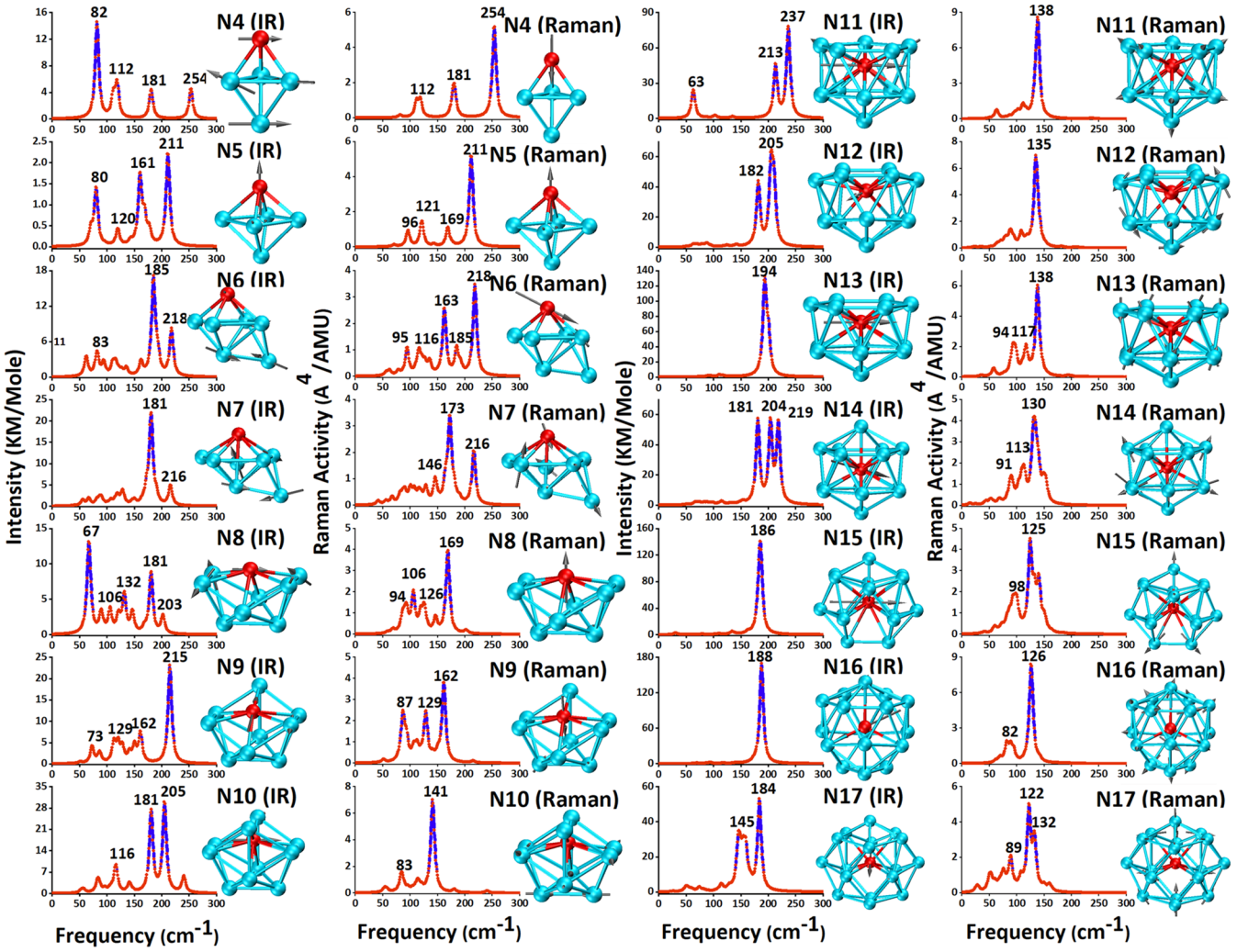

Figure 5. Infrared and Raman spectra for the ground-state structures of neutral $ZrSn_n$ (n = 4−17) species.

is the maximal location of the first peak, are located too far apart in the experimental spectrum. This increases the possibility of burying the two low-intensity peaks. All of these verify that the lowest-energy species are truly global minimal architectures detected in the experiments and also verify that our computing scheme is extremely reliable.

The computed PES of the $ZrSn_n^-$ (n = 4−17) species and the available experimental PES of the $ZrSn_n^-$ (n = 15−17) species are depicted in Figure 4; the former's peaks corresponding to each orbital showed a full width at half-maximum (fwhm) of 0.25 eV. As observed in Figure 4, no experimental counterparts of the $ZrSn_n^-$ (n = 4−14) species can be provided for comparison. As for **A4**, the computed PES showed four distinct peaks (X, A to C) lying at 2.15, 2.50, 3.33, and 3.77 eV, respectively. The spectrum of **A5** had two strongly resolved peaks (X and A) located at 2.65 and 3.12 eV, respectively, and two weak shoulder peaks (B and C) located at 3.63 and 3.85 eV, respectively. **A6** had one shoulder peak (X) and two resolved peaks (A and B), respectively, residing at 2.77, 3.10, and 4.06 eV. **A7** had two sharp peaks (X and A) and

https://doi.org/10.1021/acsomega.3c07674
ACS Omega 2024, 9, 3675−3690

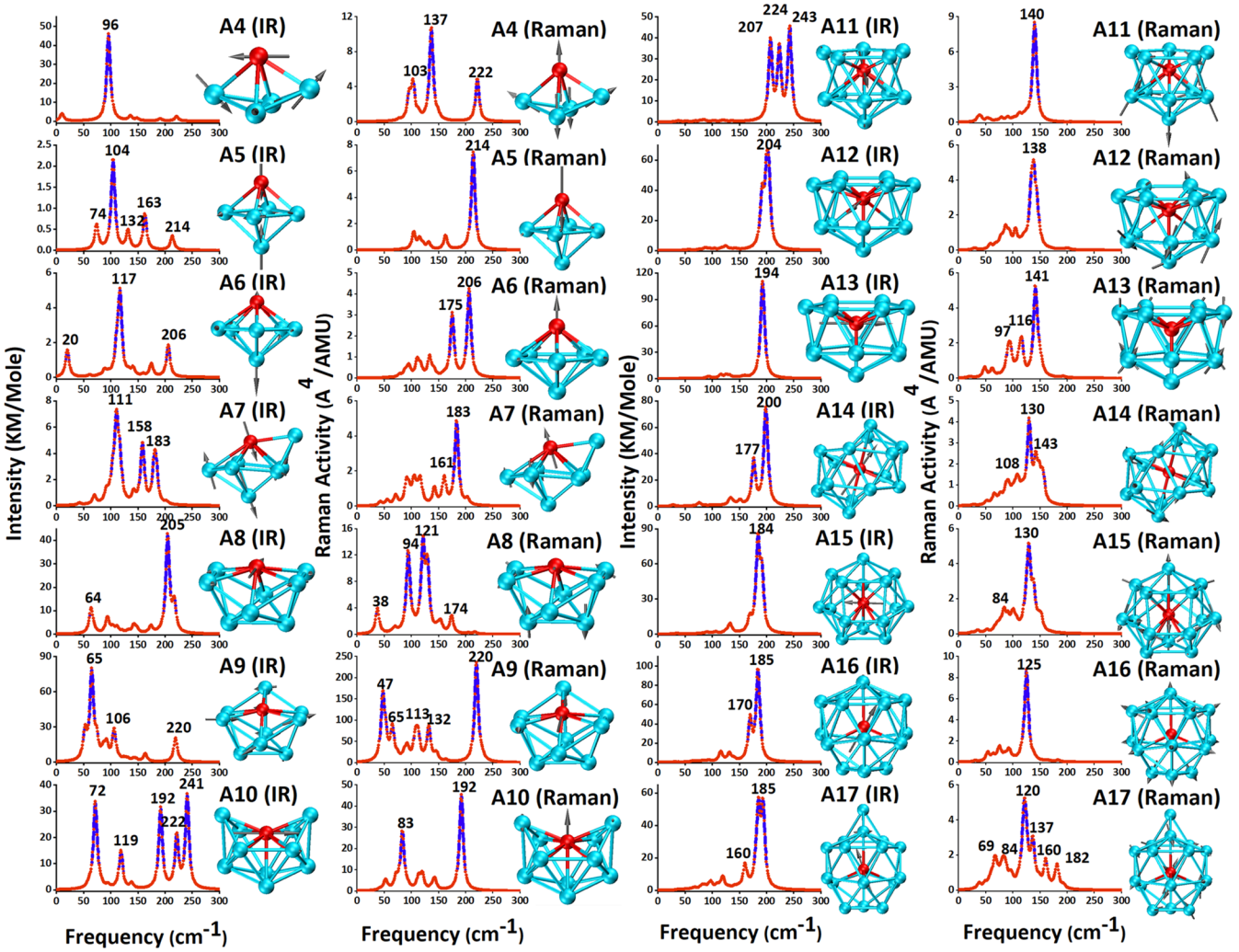

Figure 6. Infrared and Raman spectra for the ground-state structures of anionic $ZrSn_n^-$ (n = 4−17) species.

two weak peaks (B and C) residing at 2.94, 3.46, 3.89, and 4.56 eV, respectively. **A8** had two broad band peaks (X and A) and one distinct peak (C), situated at 2.87, 3.27, and 4.53 eV, respectively. **A9**'s geometry exhibited five feature peaks, including two sharp peaks (A and B) and three weak peaks (X, C, and D), seated at 3.38 and 3.83 eV, 2.79, 4.30, and 5.12 eV from small to large, respectively. For n = 10, four feature peaks (X, A to C) were observed in the spectrum, located at 3.00, 3.56, 4.05, and 4.98 eV, respectively. **A11** displayed one distinct peak (X) and five adjacent peaks (A to E) at 2.70, 3.55, 4.11, 4.66, 5.11, and 5.60 eV, respectively. The spectrum of **A12** showed three weak peaks and two sharp peaks seated at 3.23, 4.98, 5.41 eV and 3.93, 4.46 eV, respectively. In the case of **A13**, there were four peaks (X, A to C) residing at 2.66, 3.90, 4.75, and 5.13 eV, respectively. In the case of **A14**, there were four well-resolved peaks (X, A to C) situated at 3.39, 4.01, 4.80, and 5.29 eV, respectively. The simulated PES of **A15** can be observed as displaying one small peak (X) and two peaks (A and B) centered at 2.92, 4.01, and 4.71 eV, which excellently matched the experimental peaks situated at 3.11, 4.13, and 4.74 eV, respectively. It can seen that the simulated spectrum of **A16** shows a small bump labeled as X, one distinctly strong peak labeled as A, and four shoulder peaks labeled as B, C, D, and E. The five peaks are centered at 2.19, 3.85, 4.47, 4.82, 5.12, and 5.60 eV, which are in excellent accordance with the experimental data of 2.25, 3.99, 4.48, 4.95, 5.23, and 5.69 eV, respectively. The two detailed peaks of **A17** in the computed PES are centered at 2.60 and 3.04 eV (X and A) and they have no measured counterparts. The latter three broad simulated peaks (B to D) of **A17** are located at 3.90, 4.58, and 5.30 eV, in good accordance with the experimental peaks at 4.05, 4.67, and 5.39 eV. It can be observed that the simulated spectra of the lowest-energy structures are more in agreement with the experimental features as per the above discussion. In Figure S4 in the Supporting Information, simulated PES for the global minimum structures at PBE0, B3LYP, and CAM-B3LYP functionals compared with measured spectra also are provided. It can be obviously observed that the PES of the global minimum structures at the three functionals are supremely similar and in agreement with the experimental ones. For n = 17, two small peaks are detected in the simulated spectra by all three functionals, which confirms our above point of view that it is possibly due to the burying of the two low-intensity peaks in previous measurements. Apart from these, additional PES for the global and local minimum structures (Figure S5) and their peaks' values (Table S1) are provided for the PBE0 functional. It can be obviously observed that the simulated PES of the local minimum structures are in disagreement with those of the global structures, especially with the measured spectra at n = 15−17. Therefore, the

https://doi.org/10.1021/acsomega.3c07674
ACS Omega 2024, 9, 3675−3690

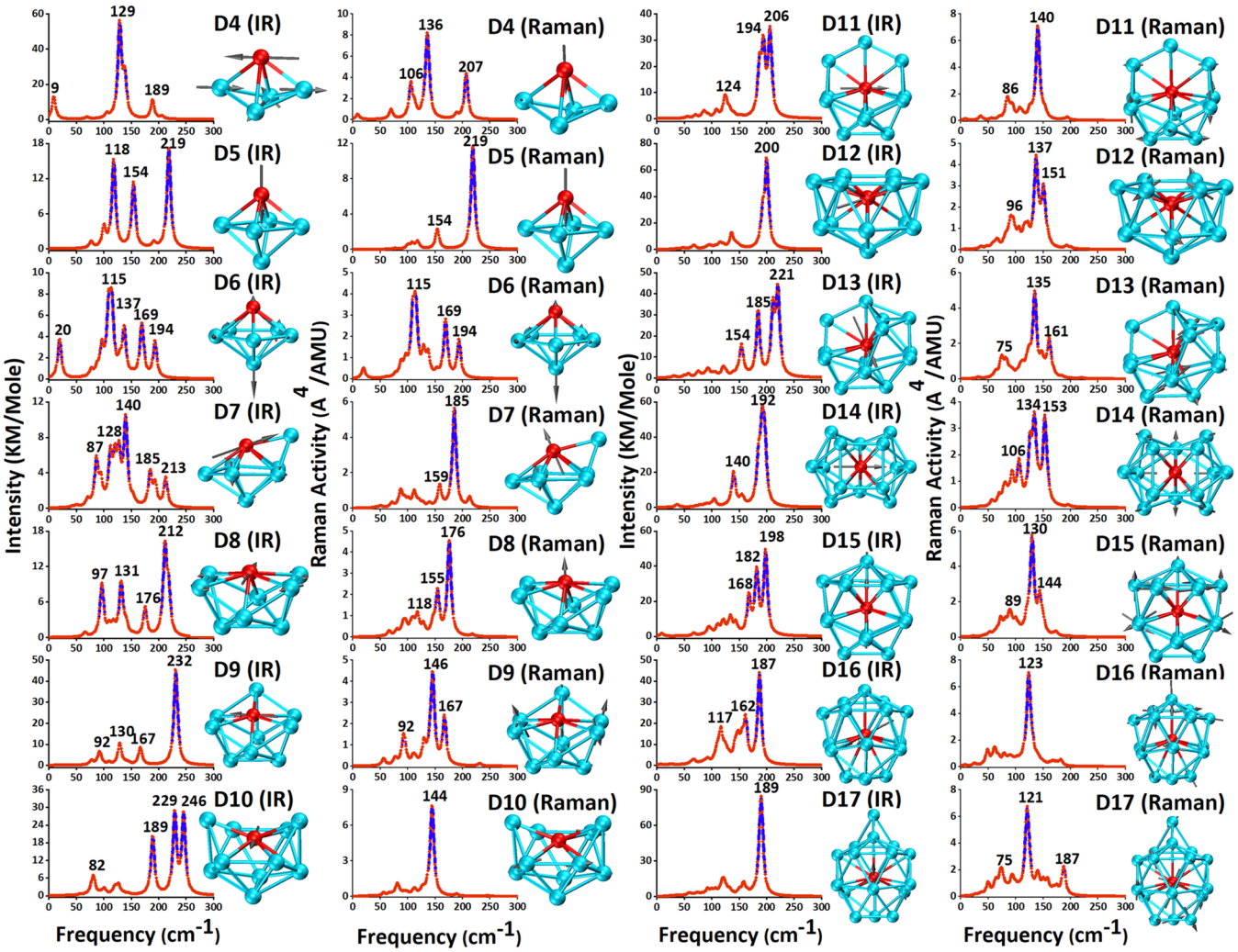

Figure 7. Infrared and Raman spectra for the ground-state structures of dianionic $ZrSn_n^{2-}$ (n = 4−17) species.

simulated spectra are in satisfactory accordance with the experimental PES, which signifies that the current ground-state structures are the dominant species in the experiments; we hope that our theoretical simulations will provide useful information for further experimental research.

In Figures 5, 6, and 7, the simulated infrared and Raman spectra, which can be used to provide the spectral information including frequencies and intensities, as well as the vibrational modes of architectures of the neutral, anionic, and dianionic lowest-energy $ZrSn_n^{0/-/2-}$ (n = 4−17) clusters, are presented. The gray arrows not only present the vibrational displacement direction for each atom, but their proportion of length also presents the proportion of vibrational displacement of each atom. The frequencies and modes of the three species are summarized in Tables S2−S4. In terms of neutral **N4**, the highest intense infrared and Raman vibrational frequency is, respectively, located at 82 cm^{-1} with bending mode and at 254 cm^{-1} with stretching mode between the Zr atom and Sn_3-triangle framework along the main axis. For anion, the in-place rocking mode located at 96 cm^{-1} belongs to **A4** with the highest intense infrared frequency, and the symmetric stretching mode located at 137 cm^{-1} belongs to **A4** with the strongest Raman frequency. For the **D4** cluster, among the vibrational modes of the highest intense infrared active, the rocking mode is located at 129 cm^{-1}. For Raman frequency, the stretching mode is located at 136 cm^{-1}, perpendicular to the distorted Sn_4-rhombus. For n = 5, the strongest infrared and Raman peaks of **N5** are both situated at 211 cm^{-1}, and so are those of **D5** both at 219 cm^{-1}, all belonging to the stretching mode between the Zr atom and Sn_5 framework along the main axis. The most prominent infrared peak of **A5** spectra at 104 cm^{-1} belongs to the stretching mode for the entire framework along the main axis, and the strongest Raman peak situated at 214 cm^{-1} belongs to the stretching modes of the Zr to Sn_5 framework in accordance with those of **N5** or **D5**. The strongest peak in the infrared spectra of **N6** species at 185 cm^{-1} belongs to deformation vibration, and that in the Raman spectra of the **N6** species at 218 cm^{-1} belongs to stretching vibration. In **A6** spectra, the strongest peak with infrared active is situated at 117 cm^{-1} with stretching vibration for the entire framework, and that with Raman active is situated at 206 cm^{-1} with the stretching mode of the Zr atom to Sn_6 framework, respectively. One dominant frequency in both infrared and Raman spectra of the **D6** species can be seen at 115 cm^{-1} with stretching vibration for the entire framework. For **N7**, the vibrational mode at 181 cm^{-1} with infrared active is wagging vibration, and that at 173 cm^{-1} with Raman active is twisting vibration. The most dominant infrared vibrational wave of **A7** and **D7** is, respectively, located at 111 cm^{-1} with scissoring vibration and at 140 cm^{-1} with asymmetric

https://doi.org/10.1021/acsomega.3c07674
ACS Omega 2024, 9, 3675−3690

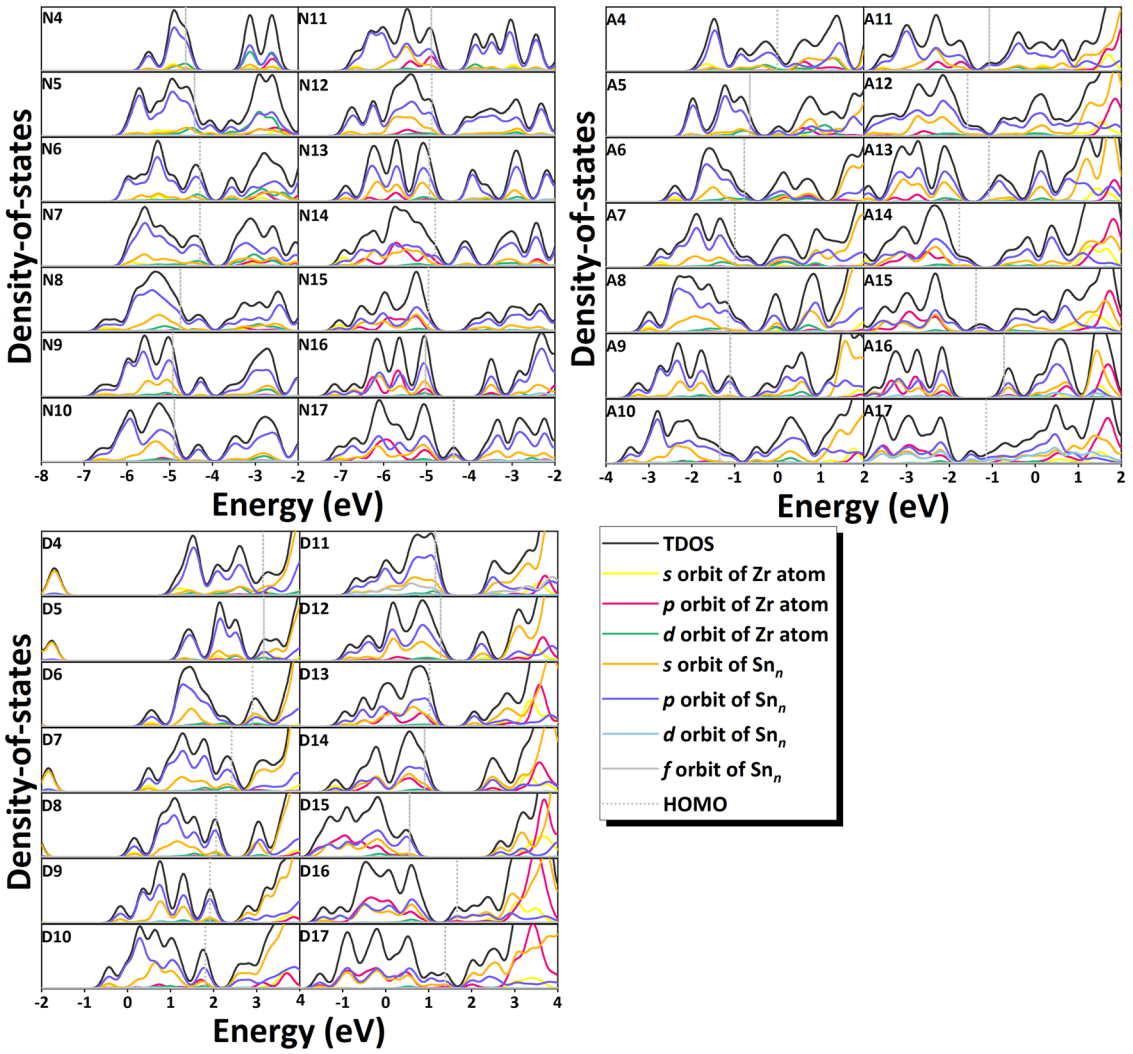

Figure 8. TDOS and PDOS curves of the most stable neutral, anionic, and dianionic $ZrSn_n^{0/-/2-}$ (n = 4−17) species.

stretching vibration, and the most dominant Raman vibrational frequency of both **A7** and **D7** is in stretching vibration between the Zr atom and Sn_7 framework, respectively situated at 183 cm^{-1} and 185 cm^{-1}. For **N8**, the strongest peak in the infrared spectra is at 67 cm^{-1}, resulted from the asymmetric stretching vibration, and that in the Raman spectra of **N8** is at 169 cm^{-1}, resulted from the stretching vibration between the Zr atom and Sn_8 framework, which is in accordance with the vibrational mode in the Raman spectra of **D8** at 176 cm^{-1}. The most dominant infrared vibrational wave of **A8** located at 205 cm^{-1} is the twisting vibration of the Zr atom parallel to the Sn_8 framework, which is in accordance with the vibrational mode in the infrared spectra of **D8** at 212 cm^{-1}. The most dominant Raman vibrational frequency of **A8** at 121 cm^{-1} is the symmetric stretching vibration of the Sn_8 framework. For **N9**, the vibration mode at the highest frequency of 215 cm^{-1} with infrared active is the twisting mode of the Zr atom parallel to the Sn_9 framework, which is in accordance with the vibrational mode of **A9** with the most intense Raman active at 220 cm^{-1} and the vibrational mode of **D9** with the most intense infrared active at 231 cm^{-1}. The strongest peak of **N9** with Raman active is located at 162 cm^{-1} with the stretching vibration between the Zr atom and Sn_9 framework. The strongest peak of **A9** with infrared active is located at 65 cm^{-1} for the asymmetric stretching vibration of the Sn_9 framework and the strongest peak of **D9** with Raman active is located at 146 cm^{-1} for the symmetric stretching vibration of the Sn_9 framework. For **N10**, **A10**, and **D10**, the vibration mode at the highest frequency with infrared active is the twisting mode of the Zr atom parallel to the Sn_{10} framework, located at 205, 241, and 229 cm^{-1}, respectively. The strongest wave situated at 141 cm^{-1} of **N10** and at 144 cm^{-1} of **D10** is the breathing vibration for the Sn_{10} framework at Raman vibration. For **A10**, the vibration mode at the highest frequency of 192 cm^{-1} with Raman active is the stretching mode between the Zr atom and Sn_{10} framework.

All neutral, anionic, and dianionic species of $ZrSn_n^{0/-/2-}$ (n = 11−17) can be summarized as follows: their most intense vibration modes with infrared active result from the deformation mode of the Zr atom in the Sn cage framework (the cage framework rarely moves). The most intense vibration modes of $ZrSn_n^{0/-/2-}$ (n = 11−17) with Raman spectra result from the breathing mode of the Sn cage framework (the Zr atom rarely moves). The most intense vibration modes with the infrared spectra of **N11** to **N17** are located at 237, 205, 194, 181, 186, 188, and 184 cm^{-1}, respectively, and the most intense vibration modes in Raman spectra are situated at 138, 135, 138, 130, 125, 126, and 122 cm^{-1}, respectively. As for

https://doi.org/10.1021/acsomega.3c07674
ACS Omega 2024, 9, 3675−3690

Table 2. NPA Valence Configurations and Magnetic Moment of Zr Atoms (in μ_B) Calculated for the Most Stable Neutral, Anionic, and Dianionic $ZrSn_n^{0/-/2-}$ (n = 4−17) Species

			magnetic moment of Zr atom					
species	electron configuration	charge (eV)	5s	4d	5p	5d	total	molecule (μ_B)
N4	$[core]5s^{0.69}4d^{3.21}5p^{0.28}5d^{0.02}$	−0.16						
N5	$[core]5s^{0.66}4d^{3.24}5p^{0.42}5d^{0.04}$	−0.33	0.04	1.20	0.02	0.01	1.27	2
N6	$[core]5s^{0.56}4d^{3.58}5p^{0.48}5d^{0.03}$	−0.62						
N7	$[core]5s^{0.50}4d^{3.60}5p^{0.52}5d^{0.04}$	−0.63						
N8	$[core]5s^{0.49}4d^{4.13}5p^{0.85}5d^{0.06}$	−1.50	0.01	0.68	0.09	0.00	0.78	2
N9	$[core]5s^{0.46}4d^{4.68}5p^{1.15}5d^{0.07}$	−2.33	0.02	0.62	0.12	0.01	0.77	2
N10	$[core]5s^{0.46}4d^{5.26}5p^{1.56}5d^{0.08}$	−3.34	0.02	0.68	0.13	0.03	0.86	2
N11	$[core]5s^{0.47}4d^{6.05}5p^{2.21}5d^{0.07}$	−4.79						
N12	$[core]5s^{0.43}4d^{5.60}5p^{1.83}5d^{0.08}$	−3.93						
N13	$[core]5s^{0.43}4d^{5.65}5p^{1.74}5d^{0.08}$	−3.89						
N14	$[core]5s^{0.47}4d^{6.12}5p^{1.99}5d^{0.09}$	−4.68						
N15	$[core]5s^{0.48}4d^{6.04}5p^{1.79}5d^{0.07}$	−4.37						
N16	$[core]5s^{0.50}4d^{6.12}5p^{1.68}5d^{0.07}$	−4.36						
N17	$[core]5s^{0.50}4d^{5.84}5p^{1.30}5d^{0.07}$	−3.70						
A4	$[core]5s^{0.60}4d^{3.40}5p^{0.43}5d^{0.03}$	−0.43	0.02	0.79	0.03	0.01	0.85	1
A5	$[core]5s^{0.70}4d^{3.40}5p^{0.51}5d^{0.03}$	−0.62	0.00	0.82	0.01	0.01	0.84	1
A6	$[core]5s^{0.57}4d^{3.42}5p^{0.59}5d^{0.05}$	−0.61	0.01	0.86	0.01	0.01	0.89	1
A7	$[core]5s^{0.48}4d^{3.88}5p^{0.75}5d^{0.06}$	−1.14	0.01	0.50	0.03	0.00	0.54	1
A8	$[core]5s^{0.45}4d^{4.34}5p^{0.86}5d^{0.06}$	−1.68	0.00	−0.05	0.07	0.00	0.02	1
A9	$[core]5s^{0.41}4d^{4.69}5p^{1.23}5d^{0.08}$	−2.38	0.01	0.29	0.07	0.00	0.37	1
A10	$[core]5s^{0.43}4d^{5.30}5p^{1.68}5d^{0.09}$	−3.49	0.01	0.34	0.06	0.01	0.42	1
A11	$[core]5s^{0.44}4d^{5.98}5p^{2.07}5d^{0.10}$	−4.58	0.00	0.30	0.01	0.04	0.35	1
A12	$[core]5s^{0.41}4d^{5.53}5p^{1.69}5d^{0.09}$	−3.71	0.00	0.25	0.01	0.01	0.27	1
A13	$[core]5s^{0.41}4d^{5.56}5p^{1.60}5d^{0.08}$	−3.64	0.00	0.08	0.00	0.00	0.08	1
A14	$[core]5s^{0.45}4d^{5.96}5p^{1.82}5d^{0.08}$	−4.30	0.00	0.17	0.00	0.00	0.17	1
A15	$[core]5s^{0.47}4d^{6.03}5p^{1.73}5d^{0.09}$	−4.31	0.00	0.21	0.01	0.02	0.24	1
A16	$[core]5s^{0.48}4d^{6.05}5p^{1.53}5d^{0.10}$	−4.15	0.00	0.22	0.01	0.03	0.26	1
A17	$[core]5s^{0.48}4d^{6.02}5p^{1.45}5d^{0.09}$	−4.03	0.00	0.17	0.01	0.01	0.19	1
D4	$[core]5s^{0.82}4d^{3.10}5p^{0.81}5d^{0.04}$	−0.79	0.36	1.02	0.39	0.01	1.80	2
D5	$[core]5s^{0.68}4d^{3.64}5p^{0.63}5d^{0.04}$	−0.97						
D6	$[core]5s^{0.73}4d^{3.30}5p^{0.80}5d^{0.06}$	−0.88	0.27	1.36	0.24	0.02	1.89	2
D7	$[core]5s^{0.44}4d^{4.01}5p^{0.80}5d^{0.06}$	−1.28						
D8	$[core]5s^{0.42}4d^{4.27}5p^{0.98}5d^{0.06}$	−1.70						
D9	$[core]5s^{0.38}4d^{4.73}5p^{1.31}5d^{0.08}$	−2.47						
D10	$[core]5s^{0.42}4d^{5.28}5p^{1.62}5d^{0.10}$	−3.40						
D11	$[core]5s^{0.36}4d^{5.21}5p^{1.42}5d^{0.08}$	−3.06						
D12	$[core]5s^{0.38}4d^{5.46}5p^{1.53}5d^{0.08}$	−3.45						
D13	$[core]5s^{0.40}4d^{5.92}5p^{1.76}5d^{0.08}$	−4.16						
D14	$[core]5s^{0.42}4d^{5.91}5p^{1.68}5d^{0.08}$	−4.08						
D15	$[core]5s^{0.44}4d^{5.94}5p^{1.57}5d^{0.08}$	−4.03						
D16	$[core]5s^{0.46}4d^{5.80}5p^{1.30}5d^{0.08}$	−3.63						
D17	$[core]5s^{0.47}4d^{5.93}5p^{1.33}5d^{0.09}$	−3.81						

anion, the most intense vibration modes of **A11** to **A17**, respectively, are situated at 243, 204, 194, 200, 184, 185, and 185 cm^{-1} with infrared spectra, respectively. Their most intense vibration modes are situated at 140, 138, 141, 130, 130, 125, and 120 cm^{-1} in the Raman spectra, respectively. In the case of dianion, the most intense vibration modes of **D11** to **D17**, respectively, are observed at 206, 200, 221, 192, 198, 187, and 189 cm^{-1} with infrared spectra. Their most intense vibration modes are located at 140, 137, 135, 134, 130, 123, and 121 cm^{-1} in the Raman spectra, respectively.

The neutral, anionic, and dianionic $ZrSn_n^{0/-/2-}$ (n = 4−17) species reflect various waves of spectra from infrared and Raman under the impact of architectural altering.t According to infrared analysis, it is learnt that in unsealed $ZrSn_n^{0/-/2-}$ (n = 4−10) frameworks, the strongest peaks favor the stretching mode of Zr to Sn frameworks or bending mode of Zr−Sn bonds. Encapsulated $ZrSn_n^{0/-/2-}$ (n = 11−17) configurations show the degenerated deformation mode of Zr atom wagging in the Sn cage framework (the cage framework rarely moves). With Raman actives, for unsealed $ZrSn_n^{0/-/2-}$ (n = 4−10) frameworks, the stretching mode of Zr to Sn frameworks or bending mode of Zr−Sn bonds also favors the strongest peaks. It is the breathing mode of the Sn cage framework (the Zr atom rarely moves) for encapsulated $ZrSn_n^{0/-/2-}$ (n = 11−17) configurations. As far as it can be observed, particularly for anions, there are multiple absorptions at the beginning, but they generally have fewer or only one strong peak upon structural growth. The strongest peaks of the infrared and Raman spectra are red-shifted from n = 11 to 17. One benefit is that these $ZrSn_n^{0/-/2-}$ (n = 4−17) species may be advanta-

https://doi.org/10.1021/acsomega.3c07674
ACS Omega 2024, 9, 3675−3690

geous for far-infrared sensing devices because these vibration waves are presented in the infrared range of these clusters in the 400−10 cm^{-1} far-infrared region.

3.3. Electronic Properties: DOS, NPA, and Charge Transfer. In order to analyze the electronic configuration information on the $ZrSn_n^{0/-/2-}$ (n = 4−17) clusters, the TDOS of neutral, anionic and dianionic clusters, and PDOS were calculated, which could yield some important information like the contributions of atoms or fragments of molecules, and the interactions in the orbital. The DOS of valence shell molecule orbits is depicted in Figure 8. The Gaussian function with a fwhm of 0.30 eV was used for broadening the molecular orbital energies to yield the DOS curves. As for neutral and anionic $ZrSn_n^{0/-}$ clusters, when n = 4−10, the molecular orbits are dominantly contributed from the p electrons of the host of Sn_n skeletons near the highest occupied molecular orbital (HOMO), while the contributions of the s electrons of Sn_n and the d electrons of Zr atom are relatively less. But when n = 11−17, in addition to the above electrons, the molecular orbits are also obviously contributed from the p electrons of the Zr atom. The molecular orbits obviously comprise the contribution of the p electrons of Zr atom for dianionic clusters, which happens when n = 4−12 and when n = 13−17. The boundary is consistent with the geometry evolution for the transition between exo- and endohedral patterns. Their overlapping indicates that spd hybridization is a dominant contribution to formatting the molecular orbits. From Figure S6, it can be observed that there is a distinct profile difference between α-TDOS and β-TDOS, illustrating that the spin polarization is extremely significant.

Apart from that, NPA was further done to comprehend the interaction between the Zr atom and the Sn_n skeletons, including the valence electronic shell configurations (5s, 4d, 5p, and 5d state) on the Zr atom and total magnetic moments of Zr atom and clusters, listed in Table 2. The results of NPA indicate that the valence electronic configuration of the Zr atom of the $ZrSn_n^{0/-/2-}$ (n = 4−17) clusters is $5s^{0.36-0.82}4d^{3.10-6.12}5p^{0.28-2.21}5d^{0.02-0.10}$. The valence electronic configuration of the Zr atom indicated that the s, p, and d orbits have got or lost some charge. Aside from the PDOS in Figure 8, the TDOS profile is composed of the PDOS including s, p, and d orbits, which reflects the contributions of the fragments. The two approaches confirm that the valence orbits of Zr atoms constitute spd hybrid orbits in the clusters, matching with the DOS analysis. The interaction between these hybrid orbits and the valence orbits of the Sn atoms results in the clusters remaining in a stable state.

Furthermore, charge transfer was investigated for the bonding interaction between the Zr atom and the host of the tin clusters; its alteration for $ZrSn_n^{0/-/2-}$ (n = 4−17) clusters actually correlates with the geometric evolution, as shown in Figure 9. The charge transfer chart indicates that Zr atoms always serve as electron acceptors in clusters. It can be seen from the figure that the variation tendencies of charge transfer in neutral, anionic, and dianionic clusters are consistent in total, except for $ZrSn_{11}^{2-}$ and $ZrSn_{12}^{2-}$. When n = 4 to 7, the charge transfer increases slowly from the Sn_n framework to the Zr atom ranged from −0.16 to −1.28 eV, suggesting that the characteristics of bonding between Zr and tin nanoalloys may be mixed with ionic bonds and covalent bonds. Starting from n = 7, the charge transfer increases considerably, ranging from −1.50 to −4.79 eV from tin clusters to Zr atoms along with the increment of the number of Sn atoms, suggesting that the characteristics of bonding between Zr and tin nanoalloys may be mixed with ionic bonds and covalent bonds. Until reaching the maximum charge transfer (about 4 eV) at n = 11 for neutral and anion, as well as at n = 13 for dianion, the nature of the bonding between Zr atoms and tin nanoalloys is metallic bonds. The charge transfer from tin cage frameworks to Zr atoms is maintained at −3.63 to −4.68 eV. As a result, the electronic structure and properties indicate that the interaction between the Zr atom and Sn_n frameworks of capsulated compounds has been developing stronger than for unsealed compounds following the geometrical evolution.

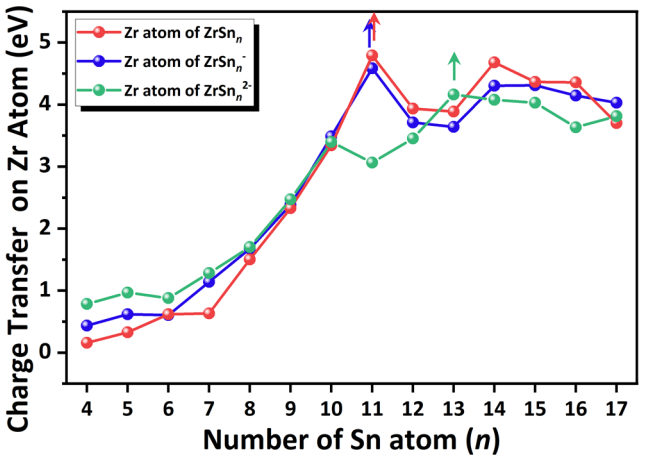

Figure 9. Size dependences of charge transfer on the Zr atom (eV) for the most stable neutral, anionic, and dianionic $ZrSn_n^{0/-/2-}$ (n = 4−17) species.

3.4. Thermodynamic and Chemical Stability. The relative stability of $ZrSn_n^{0/-/2-}$ (n = 4−17) species, including dissociation energy (DE), second energy difference (Δ^2E), and energy difference between the highest occupied molecular orbital (HOMO) and the lowest unoccupied molecular orbital (LUMO) (i.e., the HOMO−LUMO gap) (E_{gap}), was investigated to apprehend the cooperation effect of the geometric and electronic structural factors of the three species, as depicted in Figure 10.

The DE values were determined from the equations for the Zr atom and tin skeleton bonding stability, which are the following

$$E_{DE}(ZrSn_n) = E(Zr) + E(Sn_n) - E(ZrSn_n) \quad (3)$$

$$E_{DE}(ZrSn_n^-) = E(Zr) + E(Sn_n^-) - E(ZrSn_n^-) \quad (4)$$

$$E_{DE}(ZrSn_n^{2-}) = E(Zr) + E(Sn_n^{2-}) - E(ZrSn_n^{2-}) \quad (5)$$

where $E(Zr)$, $E(Sn_n)$, $E(Sn_n^-)$, $E(Sn_n^{2-})$, $E(ZrSn_n)$, $E(ZrSn_n^-)$, and $E(ZrSn_n^{2-})$ present the total energies of the respective atom or species. As plotted in Figure 10a, the DE curves of the three species all have a rising tendency due to the Zr atom being connected with more Sn atoms, while the three species interestingly race each other. The maximum DE values of neutral, anion and dianion types are situated at n = 16, 16, and 15, respectively. This indicates that neutral $ZrSn_{16}$, anionic $ZrSn_{16}^-$, and dianionic $ZrSn_{15}^{2-}$ have the best enhancement stability effect on doping Zr atoms into tin clusters. Among all of them, **N16** has the best inherent stability.

https://doi.org/10.1021/acsomega.3c07674
ACS Omega 2024, 9, 3675−3690

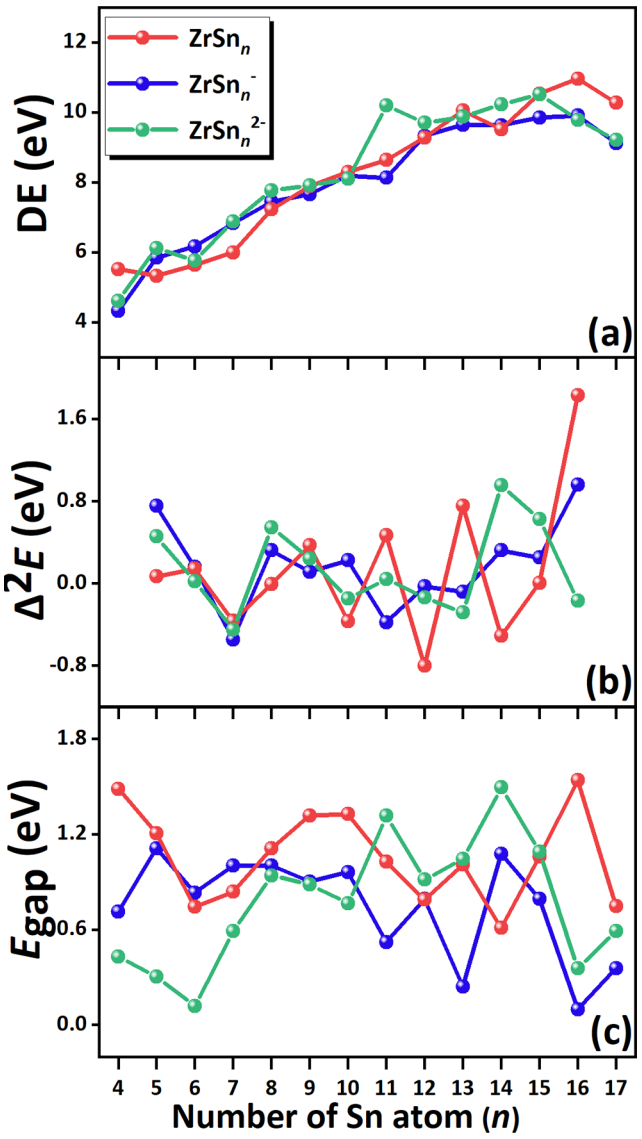

Figure 10. Size dependences of (a) DE; (b) Δ^2E; and (c) E_{gap} for the most stable neutral, anionic, and dianionic $ZrSn_n^{0/-/2-}$ (n = 4−17) species.

The Δ^2E, which versus the corresponding cluster size is plotted in Figure 10b, is associated with its two directly adjacent ones, conventionally calculated as follows

$$\Delta^2E(ZrSn_n) = E(ZrSn_{n-1}) + E(ZrSn_{n+1}) - 2E(ZrSn_n) \quad (6)$$

$$\Delta^2E(ZrSn_n^-) = E(ZrSn_{n-1}^-) + E(ZrSn_{n+1}^-) - 2E(ZrSn_n^-) \quad (7)$$

$$\Delta^2E(ZrSn_n^{2-}) = E(ZrSn_{n-1}^{2-}) + E(ZrSn_{n+1}^{2-}) - 2E(ZrSn_n^{2-}) \quad (8)$$

It can be found that five remarkable peaks appear for the neutral type at n = 6, 9, 11, 13 and 16, and for the anion type at n = 8, 10, 12, 14 and 16; for the dianion type, the peaks appear at n = 8, 11, and 14. Among all of them, **N16** has the best relative stability.

E_{gap} is an important physical parameter, larger values of which indicate better photochemical stability. Baerends et al.[62] expounded that the E_{gap} calculated via pure DFT numerically fits the real optical gap instead of hybrid DFT. It is based on the fact that the energies of HOMO and LUMO predicted by Kohn−Sham molecular orbital approximations go through a similar quantity upshift as a whole, while Hartree−Fock (HF) functional moves the LUMO up to much higher energy levels than the HOMO. Therefore, PBE functional was engaged to evaluate the E_{gap} of the $ZrSn_n^{0/-/2-}$ (n = 4−17) species. As can be seen in Figure 10c, the E_{gap} of the $ZrSn_n^{0/-/2-}$ (n = 4−17) species is assessed at PBE functional. The E_{gap} curves of neutral, anionic, and dianionic types range from 0.61 to 1.54 eV, from 0.10 to 1.11 eV, and from 0.12 to 1.49 eV, respectively. The neutral, anionic, and dianionic type denotes local maximum values located at n = 10, 13, and 16, n = 5, 7, 10, 12, and 14, and n = 8, 11, and 14. Among all of them, **N16** has the best chemical stability, at 1.54 eV, which matches with the experimental value (1.64 eV) of Nakajima et al.[37] From all of these, it can be concluded that the neutral $ZrSn_{16}$ nanoscale compound possesses both thermodynamic and chemical stability.

3.5. Neutral $ZrSn_{16}$ Nanoscale Compound: MO Analysis and UV−Vis Spectra. MO analysis was performed to further study the chemical bonding nature of the neutral $ZrSn_{16}$ compounds, which possess outstanding stability. Based on the foundation of the spherical jellium model, the 68 magic number valence electron shell model of $ZrSn_{16}$ is $[1S^21P^61D^{10}1F^{14}2S^21G^{14}2P^61G^42D^{10}]$, resulting in the most stable geometrical and electronic configuration with high T_d-symmetry, as shown in Figure 11.

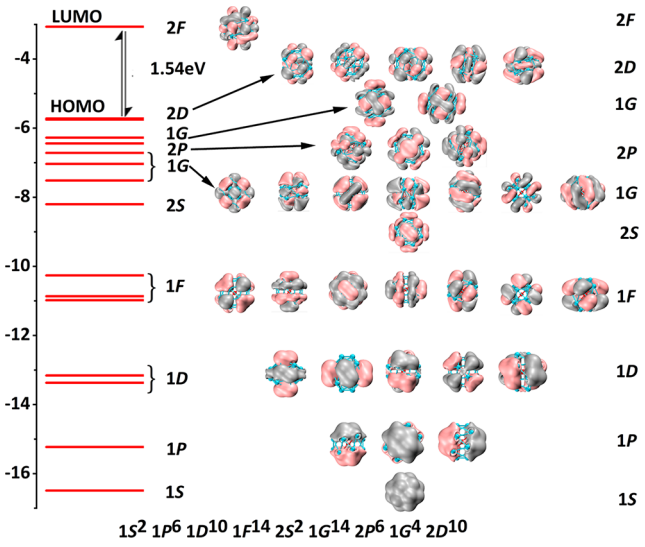

Figure 11. MOs maps and energy levels of the highest and higher occupied molecular orbital of the neutral $ZrSn_{16}$ compound.

The UV−vis spectra were simulated to further comprehend the optical properties of $ZrSn_{16}$ clusters. The 120 excited states were calculated to satisfy the accuracy and sufficiency of excited states of the object of study via LANL2TZ and aug-cc−PVTZ-PP basis sets for Zr atom and Sn atoms, respectively, at time-dependent DFT (TDDFT) with PBE functional. With a fwhm value of 0.20 eV, the discrete lines corresponding to each transition mode (absorption peaks) are broadened. The oscillator strength is represented by the gray straight lin, and

https://doi.org/10.1021/acsomega.3c07674
ACS Omega 2024, 9, 3675−3690

the transition strength is interpreted by the height of the line. From Figure 12, the underlying characteristic of the total UV−vis spectrum (black curve) of $ZrSn_{16}$ neutral is very clear, which produces four absorption bands, including three strongest absorption peaks positioned at 391, 423, 465, and 569 nm in the visible region respectively, and one positioned at 734 nm in the near-infrared region. The first absorption band is from 360 to 403 nm. The first peak is at 391 nm. The second peak is at 423 nm and its absorption band is from 403 to 450 nm. The third absorption band, with the strongest peak at 465 nm, is from 450 to 517 nm. The fourth absorption band having the range of 517−639 nm has the most intense peak at 569 nm. The firth absorption band, with the strongest peak at 734 nm, is from 639 to 869 nm. The summit of 391 nm is composed of $S_0 \rightarrow S_{118}$ transitions with the contribution of 96.17%. The summit of 423 nm has two parts composed of $S_0 \rightarrow S_{100}$ and $S_0 \rightarrow S_{95}$, transitions with contributions of 72.94 and 22.29%, respectively. The peak of 465 nm is composed of three sections, $S_0 \rightarrow S_{56}$, $S_0 \rightarrow S_{62}$, and $S_0 \rightarrow S_{48}$ transitions with contributions of 71.04, 13.61, and 9.69%, respectively. The summit of 569 nm is made of $S_0 \rightarrow S_{19}$ transition with the contribution of 98.35%. The last peak of 734 nm is attributed to the two transitions of $S_0 \rightarrow S_{12}$ and $S_0 \rightarrow S_6$ with contributive rates 79.01 and 20.99%. In addition to the infrared region, the visible-light belt (380−700 nm) accounts for 78.31% of the total area and can be excited by natural light, especially with solar energy as the photocatalyst. At the same time, UV−vis spectra were calculated using TDDFT with PBE, PBE0, B3LYP, and CAM-B3LYP functionals, in order to analyze the transitions in 120 excited states, which are enough to describe the characteristics. Figure S7 shows that the strongest absorption bands are situated in the near-ultraviolet regions. Meanwhile, the other three peaks are positioned in the visible-light region. In other words, the ultraviolet−visible spectra formed by the four functionals are very similar to each other. The FK-cage polyhedral $ZrSn_{16}$ with high T_d symmetry can be further explored as a possible optoelectronic material to be potentially used in optoelectronic devices or solar energy converters.

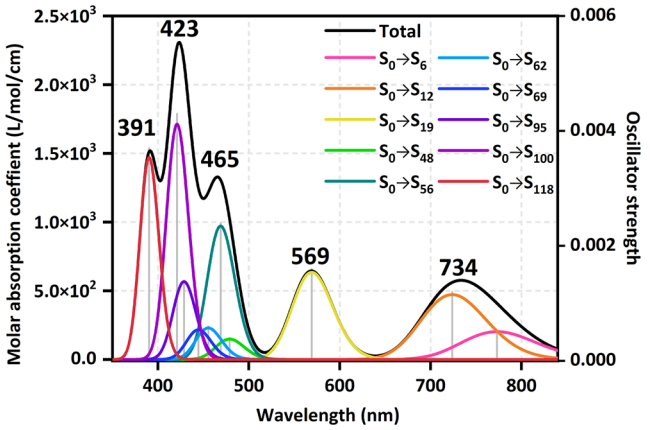

Figure 12. Calculated UV−vis spectrum of the neutral $ZrSn_{16}$ compound; solid curves and lines represent the absorption spectra and oscillator strength, respectively.

4. CONCLUSIONS

The global minimal architectures of $ZrSn_n^{0/-/2-}$ (n = 4−17) nanoscale compounds were investigated by performing the ABCluster global search approach coupled with PBE0, B3LYP, and CAM-B3LYP functionals. Regarding the architectural growth pattern of the neutral, anion, and dianion species, the $ZrSn_n^{0/-/2-}$ (n = 4−17) compounds possess two different stages of adsorption pattern. When n = 4−7, the $ZrSn_4^{0/-/2-}$ cluster as the basic unit adsorbs Sn atoms to be the larger cluster, and when n = 8−17, the $ZrSn_8^{0/-/2-}$ cluster as the basic unit adsorbs Sn atoms one by one. Among these, at n = 8−10 for the neutral and anion species, as well as at n = 8−11 for the dianionic species, the compounds belong to semi-encapsulated structures. That is to say, and up to $ZrSn_{11}^{0/-}$ and $ZrSn_{13}^{2-}$ compounds, the Zr atoms are completely encircled in the tin clusters. The simulated PES including $ZrSn_{15}^{-}$ and $ZrSn_{16}^{-}$ are in excellent agreement with the available experimental ones, as well as $ZrSn_{17}^{-}$ agrees partially with the experimental ones, which signifies that the current ground-state structures are the dominant species in the performed experiments. According to infrared and Raman analysis, it was learnt that for unsealed $ZrSn_n^{0/-/2-}$ (n = 4−10) frameworks, the strongest peaks favor the stretching mode of Zr to Sn frameworks or bending mode of Zr−Sn bonds. The encapsulated $ZrSn_n^{0/-/2-}$ (n = 11−17) configurations generated a deformation mode of Zr atom wagging in the Sn cage framework (the cage framework rarely moves) with infrared actives and a breathing mode of the Sn cage framework (the Zr atom rarely moves) with Raman actives. The results of electronic structure and properties indicate that the interaction between the Zr atom and Sn_n frameworks of capsulated compounds develops stronger than for the unsealed compounds following the geometrical evolution. The analysis of thermodynamic and chemical stability showed that the neutral $ZrSn_{16}$ nanoscale compound possesses the most preferable stability. Furthermore, the results of MOs analysis and UV−vis spectrum showed that the neutral $ZrSn_{16}$ nanoscale compound possesses preferable optoelectronic properties to be potentially used in optoelectronic devices or solar energy converters as the best building block motif for new multipurpose nanoscale materials.

■ ASSOCIATED CONTENT

Supporting Information

The Supporting Information is available free of charge at https://pubs.acs.org/doi/10.1021/acsomega.3c07674.

global and local minimum $ZrSn_n^{0/-/2-}$ (n = 4−17) clusters at PBE0, B3LYP and CAM-B3LYP functionals; simulated PES spectra of the ground-state structures compared with experimental PES for n = 15−17 at PBE0, B3LYP and CAM-B3LYP functionals; simulated PES spectra of the ground state and competed ground state structures of anion at PBE0 functional; the distinct profile differences between the α- and β-TDOS of $ZrSn_n$ possessing spin polarization at PBE0 functional; calculated UV−vis spectra of the neutral $ZrSn_{16}$ compound at PBE, PBE0, B3LYP and CAM-B3LYP functionals; and the peak data of PES, infrared and Raman spectra at PBE0 functional (PDF)

■ AUTHOR INFORMATION

Corresponding Author

Caixia Dong − *College of Resources and Environmental Engineering, Inner Mongolia University of Technology,*

https://doi.org/10.1021/acsomega.3c07674
ACS Omega 2024, 9, 3675−3690

Hohhot 010051, People's Republic of China; orcid.org/0009-0000-1161-7469; Email: dongcx@imut.edu.cn

Authors

Yanpeng Zhang − *College of Chemical Engineering, Inner Mongolia University of Technology, and Inner Mongolia Key Laboratory of Theoretical and Computational Chemistry Simulation, Hohhot 010051, People's Republic of China*

Jucai Yang − *College of Chemical Engineering, Inner Mongolia University of Technology, and Inner Mongolia Key Laboratory of Theoretical and Computational Chemistry Simulation, Hohhot 010051, People's Republic of China; College of Resources and Environmental Engineering, Inner Mongolia University of Technology, Hohhot 010051, People's Republic of China;* orcid.org/0000-0003-4998-0364

Complete contact information is available at: https://pubs.acs.org/10.1021/acsomega.3c07674

Notes

The authors declare no competing financial interest.

■ ACKNOWLEDGMENTS

This study was supported by the Program for Innovative Research Team at the University of Inner Mongolia Autonomous Region (Grant No. NMGIRT2214), by the Inner Mongolia Natural Science Foundation (Grant No. 2022MS02001), by the Basic Scientific Research Projects of Universities in Inner Mongolia Autonomous Region (Grant No. JY20220025, No. JY20220042, and No. JY20220359), and by the Key Laboratory of Environmental Pollution Control and Remediation at Universities of Inner Mongolia Autonomous Region.

■ ABBREVIATIONS

DFT, density functional theory; ABCluster, artificial bee colony algorithm for cluster; PES, photoelectron spectra; DOS, density of states; TDOS, total density of states; PDOS, partial density of states; NPA, natural population analysis; MOs, molecular orbital shell; UV−vis spectrum, ultraviolet−visible absorption spectrum; VDE, vertical detachment energy; AEA, adiabatic electron affinity; fwhm, full width at half-maximum; HOMO, highest occupied molecular orbital; DE, dissociation energy; Δ^2E, second energy difference; E_{gap}, energy difference between the highest occupied molecular orbital (HOMO) and the lowest unoccupied molecular orbital (LUMO) (i.e., the HOMO−LUMO gap); HF, Hartree−Fock

■ REFERENCES

(1) Barcaro, G.; Monti, S.; Sementa, L.; Carravetta, V. Atomistic Modelling of Si Nanoparticles Synthesis. *Crystals* **2017**, *7* (2), No. 54, DOI: 10.3390/cryst7020054.

(2) Liu, B.; Wang, X.; Yang, J. Comparative research of configuration, stability and electronic properties of cationic and neutral $[AuGe_n]^{\lambda}$ and $[Ge_{n+1}]^{\lambda}$ (n = 1−13, λ = 0, + 1) nanoalloy clusters. *Mater. Today Commun.* **2021**, *26*, No. 101989.

(3) Yang, Z.; Cao, Z.; Rehman, A. U.; Yang, J. Structural Evolution, Electronic Structures, and Vibrational Properties of Anionic $LuGe_n$ (n = 5−17) Clusters: From Lu-Linked to Lu-Encapsulated Configurations. *Inorg. Chem.* **2021**, *60* (18), 14446−14456.

(4) Yang, Z.; Rehman, A. U.; Cao, Z.; Yang, J. Structural evolution, photoelectron spectra and vibrational properties of anionic $GdGe_n^-$ (n = 5−18) nanoalloy clusters: a DFT insight. *RSC Adv.* **2022**, *12* (34), 22020−22030.

(5) Schäer, S.; Assadollahzadeh, B.; Mehring, M.; Schwerdtfeger, P.; Schäfer, R. Structure and electric properties of Sn_N clusters (N = 6−20) from combined electric deflection experiments and quantum theoretical studies. *J. Phys. Chem. A* **2008**, *112* (48), 12312−12319.

(6) Rajesh, C.; Majumder, C.; Rajan, M. G. R.; Kulshreshtha, S. K. Isomers of small Pb_n clusters (n = 2−15): Geometric and electronic structures based on *ab initio* molecular dynamics simulations. *Phys. Rev. B* **2005**, *72* (23), No. 235411.

(7) Lu, Z.-Y.; Wang, C.; Ho, K. Structures and dynamical properties of C_n, Si_n, Ge_n, and Sn_n clusters with n up to 13. *Phys. Rev. B* **2000**, *61*, 2329−2334.

(8) Shvartsburg, A. A.; Jarrold, M. F. Transition from covalent to metallic behavior in group-14 clusters. *Chem. Phys. Lett.* **2000**, *317*, 615−618.

(9) Assadollahzadeh, B.; Schäfer, S.; Schwerdtfeger, P. Electronic properties for small tin clusters Sn_n ($n \leq 20$) from Density Functional Theory and the Convergence Toward the Solid State. *J. Comput. Chem.* **2010**, *31* (5), 929−937.

(10) Cui, L.; Huang, X.; Wang, L.; Li, J.; Wang, L. Pb_{12}^{2-}: Plumbaspherene. *J. Phys. Chem. A* **2006**, *110*, 10169−10172.

(11) Zhao, J.; Du, Q.; Zhou, S.; Kumar, V. Endohedrally Doped Cage Clusters. *Chem. Rev.* **2020**, *120* (17), 9021−9163.

(12) Cui, L.; Huang, X.; Wang, L.; Zubarev, D.; Boldyrev, A. I.; Li, J.; Wang, L. Sn_{12}^{2-}: Stannaspherene. *J. Am. Chem. Soc.* **2006**, *128*, 8390−8391.

(13) Lehr, A.; Rivic, F.; Jäger, M.; Gleditzsch, M.; Schäfer, R. Optical absorption and shape transition in neutral Sn_N clusters with $N \leq 40$: a photodissociation spectroscopy and electric beam deflection study. *Phys. Chem. Chem. Phys.* **2022**, *24* (19), 11616−11635.

(14) Wu, D.; Du, Q.; Wu, X.; Shi, R.; Sai, L.; Liang, X.; Huang, X.; Zhao, J. Evolution of atomic structures of Sn_N, Sn_N^-, and Sn_NCl^- clusters (N = 4−20): Insight from *ab initio* calculations. *J. Chem. Phys.* **2019**, *150* (17), No. 174304.

(15) Cui, L.; Wang, L.; Wang, L. Evolution of the electronic properties of Sn_n^- clusters (n = 4−45) and the semiconductor-to-metal transition. *J. Chem. Phys.* **2007**, *126* (6), No. 064505.

(16) Zang, Q.; Chen, G.; Qin, W.; Zhao, L.; Lü, W. Comparison of Sn_n (n = 2−15) Neutral and Ionic Structures. *Chem. Res. Chin. Univ.* **2013**, *29* (3), 579−583.

(17) Li, H.; Chen, W.; Wang, F.; Sun, Q.; Guo, Z. X.; Jia, Y. Tin clusters formed by fundamental units: a potential way to assemble tin nanowires. *Phys. Chem. Chem. Phys.* **2013**, *15* (6), 1831−1836.

(18) Cui, L.; Huang, X.; Wang, L.; Li, J.; Wang, L. Endohedral Stannaspherenes $M@Sn_{12}^-$: A Rich Class of Stable Molecular Cage Clusters. *Angew. Chem., Int. Ed.* **2007**, *46* (5), 742−745.

(19) Leyva, P. G.-A.; Sosa-Hernández, E. M.; Montejano-Carrizales, J. M.; Aguilera-Granja, F. Stable geometries and magnetic properties of neutral Sn_{x+1} and $FeSn_x$ ($x \leq 8$) clusters. *Eur. Phys. J. D* **2015**, *69* (2), No. 51, DOI: 10.1140/epjd/e2015-50804-6.

(20) Shi, S.-P.; Zhao, X.; Liu, X.; Lei, D.; Yan, M.; Jiang, G. Structural and Electronic Properties in Titanium-Doped Stannum Clusters: Comparison with Their Anions and Cations. *J. Cluster Sci.* **2018**, *29* (5), 909−919.

(21) Shi, S.; Deng, B.; Liu, Y.; He, J.; Li, X.; Jiang, G.; Li, Y. A Study of Sn_nAl Clusters by Density Functional Theory: Comparison with Their Anions and Cations. *Phys. Status Solidi B* **2019**, *256* (12), No. 1900137.

(22) Sosa-Hernández, E. M.; Montejano-Carrizales, J. M.; Leyva, P. G. A. Geometrical shapes, stabilities and electronic behavior of small Fe_xSn_y ($x + y \leq 5$) atomic clusters. *Eur. Phys. J. D* **2015**, *69* (9), No. 212, DOI: 10.1140/epjd/e2015-60116-6.

(23) Sosa-Hernández, E. M.; Montejano-Carrizales, J. M.; Alvarado-Leyva, P. G. Stability and magnetic behavior of small Co_xSn_y ($x + y \leq 5$) atomic clusters. *J. Alloys Compd.* **2015**, *632*, 772−777.

(24) Sosa-Hernández, E. M.; Montejano-Carrizales, J. M.; Alvarado-Leyva, P. G. Global minimum structures, stability and electronic properties of small Ni_xSn_y ($x + y \leq 5$) bimetallic clusters; a DFT study. *Eur. Phys. J. D* **2016**, *70* (10), No. 208, DOI: 10.1140/epjd/e2016-70200-0.

(25) Tai, T. B.; Tam, N. M.; Nguyen, M. T. Evolution of structures and stabilities of zinc-doped tin clusters Sn_nZn, n = 1−12. Three-dimensional aromaticity of the magic clusters $Sn_{10}Zn$ and $Sn_{12}Zn$. *Chem. Phys.* **2011**, *388* (1−3), 1−8, DOI: 10.1016/j.chemphys.2011.06.041.
(26) Tai, T. B.; Nguyen, M. T. Enhanced Stability by Three-Dimensional Aromaticity of Endohedrally Doped Clusters $X_{10}M^{0/-}$ with X = Ge, Sn, Pb and M = Cu, Ag, Au. *J. Phys. Chem. A* **2011**, *115* (35), 9993−9999.
(27) Tai, T. B.; Nguyen, H. M. T.; Nguyen, M. T. The group 14 cationic clusters by encapsulation of coinage metals $X_{10}M^{+}$, with X = Ge, Sn, Pb and M = Cu, Ag, Au: Enhanced stability of 40 valence electron systems. *Chem. Phys. Lett.* **2011**, *502* (4−6), 187−193.
(28) Zhang, Y.; Li, X.; Lu, J.; Li, S.; Zhang, Y. Endohedral group-14 clusters $Au@X_{12}$ (X = Ge, Sn, Pb) and their anions: A first-principles study. *J. Mol. Liq.* **2023**, *376*, No. 121477, DOI: 10.1016/j.molliq.2023.121477.
(29) Neukermans, S.; Wang, X.; Veldeman, N.; Janssens, E.; Silverans, R. E.; Lievens, P. Mass spectrometric stability study of binary MS_n clusters (S = Si, Ge, Sn, Pb, and M = Cr, Mn, Cu, Zn). *Int. J. Mass Spectrom.* **2006**, *252* (2), 145−150.
(30) Rohrmann, U.; Schäfer, S.; Schäfer, R. Size- and Temperature-Dependent Magnetic Response of Molecular Cage Clusters: Manganese-Doped Tin Clusters. *J. Phys. Chem. A* **2009**, *113*, 12115−12121.
(31) Kumar, V.; Kawazoe, Y. Metal-doped magic clusters of Si, Ge, and Sn: The finding of a magnetic superatom. *Appl. Phys. Lett.* **2003**, *83* (13), 2677−2679.
(32) Rohrmann, U.; Schwerdtfegerb, P.; Schäfera, R. Atomic domain magnetic nanoalloys: interplay between molecular structure and temperature dependent magnetic and dielectric properties in manganese doped tin clusters. *Phys. Chem. Chem. Phys.* **2014**, *16* (43), 23952−23966.
(33) Fuchs, T. M.; Schäfer, R. Double Stern-Gerlach experiments on $Mn@Sn_{12}$: Refocusing of a paramagnetic superatom. *Phys. Rev. A* **2018**, *98* (6), No. 063411.
(34) Rohrmann, U.; Schäfer, R. Stern-Gerlach Experiments on $Fe@Sn_{12}$: Magnetic Response of a Jahn−Teller Distorted Endohedrally Doped Molecular Cage Cluster. *J. Phys. Chem. C* **2015**, *119* (20), 10958−10961.
(35) Gleditzsch, M.; Pašteka, L. F.; Götz, D. A.; Shayeghi, A.; Johnston, R. L.; Schäfera, R. Gold doping of tin clusters: exo- *vs.* endohedral complexes. *Nanoscale* **2019**, *11* (27), 12878−12888.
(36) Gleditzsch, M.; Jäger, M.; Pašteka, L.; Shayeghi, A.; Schäfer, R. Doping effects on the geometric and electronic structure of tin clusters. *Phys. Chem. Chem. Phys.* **2019**, *21* (44), 24478−24488.
(37) Furuse, S.; Koyasu, K.; Atobe, J.; Nakajima, A. Experimental and theoretical characterization of MSi_{16}^{-}, MGe_{16}^{-}, MSn_{16}^{-}, and MPb_{16}^{-} (M = Ti, Zr, and Hf): The role of cage aromaticity. *J. Chem. Phys.* **2008**, *129* (6), No. 064311.
(38) Atobe, J.; Koyasu, K.; Furusea, S.; Nakajima, A. Anion photoelectron spectroscopy of germanium and tin clusters containing a transition- or lanthanide-metal atom; MGe_n^{-} (n = 8−20) and MSn_n^{-} (n = 15−17) (M = Sc-V, Y-Nb, and Lu-Ta). *Phys. Chem. Chem. Phys.* **2012**, *14* (26), 9403−9410.
(39) Frisch, M. J.; Trucks, G. W.; Schlegel, H. B.; Scuseria, G. E.; Robb, M. A.; Cheeseman, J. R.; Scalmani, G.; Barone, V.; Mennucci, B.; Petersson, G. A.; Nakatsuji, H.; Caricato, M.; Li, X.; Hratchian, H. P.; Izmaylov, A. F.; Bloino, J.; Zheng, G.; Sonnenberg, J. L.; Hada, M.; Ehara, M.; Toyota, K.; Fukuda, R.; Hasegawa, J.; Ishida, M.; Nakajima, T.; Honda, Y.; Kitao, O.; Nakai, H.; Vreven, T.; Montgomery, J. A., Jr.; Peralta, J. E.; Ogliaro, F.; Bearpark, M.; Heyd, J. J.; Brothers, E.; Kudin, K. N.; Staroverov, V. N.; Kobayashi, R.; Normand, J.; Raghavachari, K.; Rendell, A.; Burant, J. C.; Iyengar, S. S.; Tomasi, J.; Cossi, M.; Rega, N.; Millam, J. M.; Klene, M.; Knox, J. E.; Cross, J. B.; Bakken, V.; Adamo, C.; Jaramillo, J.; Gomperts, R. E.; Stratmann, O.; Yazyev, A. J.; Austin, R.; Cammi, C.; Pomelli, J. W.; Ochterski, R.; Martin, R. L.; Morokuma, K.; Zakrzewski, V. G.; Voth, G. A.; Salvador, P.; Dannenberg, J. J.; Dapprich, S.; Daniels, A. D.; Farkas, O.; Foresman, J. B.; Ortiz, J. V.; Cioslowski, J.; Fox, D. J. *Gaussian 16*; Gaussian Inc.: Wallingford CT, 2009.
(40) Zhang, J.; Dolg, M. ABCluster: the artificial bee colony algorithm for cluster global optimization. *Phys. Chem. Chem. Phys.* **2015**, *17* (37), 24173−24181.
(41) Zhang, J.; Dolg, M. Global Optimization of Clusters of Rigid Molecules using the Artificial Bee Colony Algorithm. *Phys. Chem. Chem. Phys.* **2016**, *18* (4), 3003−3010.
(42) Zhang, J.; Glezakou, V. A.; Rousseau, R.; Nguyen, M. T. NWPEsSe: An Adaptive-Learning Global Optimization Algorithm for Nanosized Cluster Systems. *J. Chem. Theory Comput.* **2020**, *16* (6), 3947−3958.
(43) Adamo, C.; Barone, V. Toward reliable density functional methods without adjustable parameters: The PBE0 model. *J. Chem. Phys.* **1999**, *110* (13), 6158−6170.
(44) Hay, P. J.; Wadt, W. R. *Ab initio* effective core potentials for molecular calculations. Potentials for K to Au including the outermost core orbitals. *J. Chem. Phys.* **1985**, *82* (1), 299−310.
(45) Wadt, W. R.; Hay, P. J. *Ab initio* effective core potentials for molecular calculations. Potentials for main group elements Na to Bi. *J. Chem. Phys.* **1985**, *82* (1), 284−298.
(46) Lee, C.; Yang, W.; Parr, R. G. Development of the Colle-Salvetti correlation-energy formula into a functional of the electron density. *Phys. Rev. B* **1988**, *37* (2), 785−789.
(47) Becke, A. D. Density-functional thermochemistry. III. The role of exact exchange. *J. Chem. Phys.* **1993**, *98* (7), 5648−5652.
(48) Yanai, T.; Tew, D. P.; Handy, N. C. A new hybrid exchange−correlation functional using the Coulomb-attenuating method (CAM-B3LYP). *Chem. Phys. Lett.* **2004**, *393* (1−3), 51−57.
(49) Seuret-Hernández, H. Y.; Gamboa-Suarez, A.; Morera-Boado, C. A DFT study of the adsorption and surface enhanced Raman spectroscopy of pyridine on Au_{20}, Ag_{20}, and bimetallic Ag_8Au_{12} clusters. *J. Mol. Graphics Modell.* **2022**, *115*, No. 108234.
(50) Poutsma, J. C.; Moeller, W.; Poutsma, J. L.; Sweeny, B. C.; Ard, S. G.; Viggiano, A. A.; Shuman, N. S. Structures and Electron Affinities of Aluminum Hydride Clusters Al_nH (n = 3−13). *J. Phys. Chem. A* **2022**, *126* (10), 1648−1659.
(51) Paranthaman, S.; Vedamanickam, N.; Ganesan, M.; Sampathkumar, S. Structure, Stability, Electronic and Magnetic Properties of Fe_mBi_n (m + n = 2−4) Clusters: A DFT Study. *Russ. J. Phys. Chem. A* **2022**, *96* (11), 2466−2475.
(52) Tian, Z.; Song, C.; Wang, C.; Liu, Z.; Liao, R. Theoretical characterization of $(CuF)_n$ (n = 1−12) clusters. *Comput. Theor. Chem.* **2019**, *1157*, 28−33.
(53) Jin, X. X.; Du, J. G.; Jiang, G.; Luo, X.; Wang, X. W. Geometries and electronic properties of $Nb_nV^{(0,\pm1)}$ (n = 1−6) clusters studied by density-functional theory. *Eur. Phys. J. D* **2011**, *64* (2−3), 323−329.
(54) Lu, P.; Liu, G. H.; Kuang, X. Y. Probing the structural and electronic properties of bimetallic chromium-gold clusters Cr_mAu_n (m + n ≤ 6): comparison with pure chromium and gold clusters. *J. Mol. Model.* **2014**, *20* (8), No. 2385, DOI: 10.1007/s00894-014-2385-3.
(55) Roy, L. E.; Hay, P. J.; Martin, R. L. Revised Basis Sets for the LANL Effective Core Potentials. *J. Chem. Theory Comput.* **2008**, *4*, 1029−1031.
(56) Metz, B.; Stoll, H.; Dolg, M. Small-core multiconfiguration-Dirac−Hartree−Fock-adjusted pseudopotentials for post-*d* main group elements: Application to PbH and PbO. *J. Chem. Phys.* **2000**, *113* (7), 2563−2569.
(57) Peterson, K. A. Systematically convergent basis sets with relativistic pseudopotentials. I. Correlation consistent basis sets for the post-*d* group 13−15 elements. *J. Chem. Phys.* **2003**, *119* (21), 11099−11112.
(58) Tozer, D. J.; Handy, N. C. Improving virtual Kohn−Sham orbitals and eigenvalues: Application to excitation energies and static polarizabilities. *J. Chem. Phys.* **1998**, *109* (23), 10180−10189.
(59) Akola, J.; Manninen, M.; Häkkinen, H.; Landman, U.; Li, X.; Wang, L. Photoelectron spectra of aluminum cluster anions: Temperature effects and *ab initio* simulations. *Phys. Rev. B* **1999**, *60*, 11297−11300.

https://doi.org/10.1021/acsomega.3c07674
ACS Omega 2024, 9, 3675−3690

(60) Lu, T.; Chen, F. Multiwfn: A Multifunctional Wavefunction Analyzer. *J. Comput. Chem.* **2012**, *33* (5), 580−592.
(61) Humphrey, W.; Dalke, A.; Schulten, K. VMD: Visual Molecular Dynamics. *J. Mol. Graphics* **1996**, *14*, 33−38.
(62) Baerends, E. J.; Gritsenko, O. V.; van Meer, R. The Kohn-Sham gap, the fundamental gap and the optical gap: the physical meaning of occupied and virtual Kohn-Sham orbital energies. *Phys. Chem. Chem. Phys.* **2013**, *15* (39), 16408−16425.

https://doi.org/10.1021/acsomega.3c07674
ACS Omega 2024, 9, 3675−3690